

Paleomagnetic Secular Variation of Early Middle Miocene Volcanics From Vogelsberg (Germany)

Y. Chi¹  and F. Lhuillier¹ ¹Department of Earth and Environmental Sciences, Ludwig-Maximilians-Universität, Munich, Germany**Key Points:**

- Paleomagnetic directions were obtained from 162 volcanic units (1,920 samples) of the Vogelsberg, emplaced 15–18 Ma in Central Germany
- The dispersion of the virtual geomagnetic poles is suggestive of a more variable paleomagnetic field at 15–18 Ma than at 0–10 Ma
- The amplitude of paleomagnetic secular variation does not correlate with the reversal rate in studies at mid paleolatitude (40–50°)

Supporting Information:

Supporting Information may be found in the online version of this article.

Correspondence to:F. Lhuillier,
florian.lhuillier@lmu.de**Citation:**Chi, Y., & Lhuillier, F. (2025). Paleomagnetic secular variation of early middle miocene volcanics from Vogelsberg (Germany). *Journal of Geophysical Research: Solid Earth*, 130, e2024JB031007. <https://doi.org/10.1029/2024JB031007>Received 17 DEC 2024
Accepted 27 MAR 2025**Author Contributions:**

Conceptualization: F. Lhuillier
Data curation: Y. Chi
Formal analysis: Y. Chi
Funding acquisition: F. Lhuillier
Investigation: Y. Chi
Supervision: F. Lhuillier
Validation: F. Lhuillier
Writing – original draft: Y. Chi
Writing – review & editing: Y. Chi, F. Lhuillier

© 2025. The Author(s).

This is an open access article under the terms of the [Creative Commons Attribution License](https://creativecommons.org/licenses/by/4.0/), which permits use, distribution and reproduction in any medium, provided the original work is properly cited.

Abstract The Earth's magnetic field significantly changed its rate of polarity reversals over the past 200 Myr; yet it remains controversial whether these drastic changes—from a stable state of polarity during the Cretaceous Normal Superchron to more than 10 events per Myr during the Jurassic—are accompanied with similar changes in the directional variability of the field, termed paleosecular variation (PSV). In an effort to better constrain the geomagnetic behavior during the Miocene, we investigated the paleomagnetism of 162 volcanic units (1920 cores) from the Vogelsberg, the largest volcanic mountain range in Central Europe emplaced between 17.6 and 15.2 Ma. We successfully interpreted the paleodirections of 148 volcanic units, which led to a final collection of 127 independent geomagnetic records after correction for serial correlation. After removing the transitional directions, this collection passes the reversal test and yields a paleomagnetic pole located at 161.9°E and 84.5°N ($A_{95} = 3.2^\circ$, $N = 116$), which is statistically indistinguishable from the predictions of the latest apparent polar wander paths for stable Europe. Used as a proxy for PSV, the dispersion of the virtual geomagnetic poles $S_B = 19.1^\circ_{17.5^\circ}^{20.8^\circ}$ ($N = 116$) is consistent with a more variable paleomagnetic field during the Miocene relative to the past 10 Myr, as recently proposed from the analysis of the global PSV database. However, when focusing on the paleolatitudinal range 40–50° over the past 200 Myr, we failed to detect a robust correlation between S_B and the rate of polarity reversals.

Plain Language Summary Volcanic lavas, acquiring a residual magnetization during their initial cooling, are precious recorders of the Earth's magnetic field of the past. The Vogelsberg, emplaced at 15–18 Ma and consisting of several hundreds of volcanoes, is the largest volcanic mountain range in Central Europe and thus an ideal target to investigate the behavior of the Earth's magnetic field during the Miocene. In this paper, we report a paleomagnetic study of 162 volcanic units, leading to the successful determination of 127 independent geomagnetic records. By analyzing the statistical dispersion S_B of these records, we confirm the previous suggestion that the field may have been more variable during the Miocene than at 0–10 Ma. However, by examining the other available paleomagnetic studies on volcanic rocks at mid paleolatitude (40–50°) over the past 200 Myr, we failed to identify a correlation between S_B and the rate of polarity reversals, in contradiction with the predictions from numerical dynamo simulations.

1. Introduction

The paleomagnetic field, generated by convective motion in the Earth's fluid outer core (called geodynamo), stochastically switched its polarity while experiencing temporal fluctuations in direction and intensity over centennial to multi-million-year timescales (e.g., Merrill et al., 1996). When averaged over at least 100,000 years, its geometry can be approximated by a geocentric axial dipole (GAD; e.g., McElhinny, 2007), and its directional fluctuations around the GAD field during the periods of stable polarity are termed paleosecular variation (PSV; e.g., Johnson & McFadden, 2015). Over the past 200 Myr, the reversal frequency varied from nearly zero during the Cretaceous Normal Superchron (CNS; 84–121 Ma) to more than 10 occurrences per Myr during the Middle Jurassic (e.g., Gallet & Pavlov, 2016), with a rate of $\sim 5 \text{ Myr}^{-1}$ during the past 10 Myr (Ogg, 2020). Whether the changes in reversal frequency gradually or abruptly occurred is a matter of debate. Gradual changes may be explained by the time evolution of the thermal boundary conditions imposed by the mantle on the core (e.g., McFadden & Merrill, 1984), whereas abrupt changes may be the result of spontaneous bifurcations of the geodynamo (e.g., Gallet & Hulot, 1997).

The PSV of the Earth's magnetic field is usually quantified by the angular standard deviation S_B of the virtual geomagnetic poles (VGPs; Cox, 1970) obtained from (a) a sequence of lava flows in the case of a flood basalt (e.g., Lhuillier & Gilder, 2019); or (b) a collection of geographically dispersed cooling units in the case of a

monogenetic volcanic field (e.g., Lhuillier et al., 2017). To provide a robust estimate of the VGP scatter, several conditions should be fulfilled. First, 7–10 samples should be collected for each paleomagnetic site (i.e., for each lava flow or cooling unit seen as a time-independent geomagnetic horizon) in order to average out the intra-site variability and compensate for orientation errors (e.g., Cromwell et al., 2018). Second, 50–100 sites should be sampled to guarantee the statistical convergence of the VGP scatter (e.g., Lhuillier & Gilder, 2013). Third, stepwise demagnetization and principal component analysis should be used to identify the characteristic remanent magnetization (ChRM; e.g., Kirschvink, 1980). As S_B depends on paleolatitude, one strategy is to compare its value at the same paleolatitude between different geological epochs (e.g., Lhuillier & Gilder, 2019). Another strategy is to model the latitudinal dependency of S_B for a given epoch—using for instance a least-square fit (e.g., McFadden et al., 1988) or a statistical field model (e.g., Tauxe & Kent, 2004)—and to compare the values of the fitted parameters between different epochs (e.g., Engbers et al., 2024; McFadden et al., 1991). Although in principle more powerful, this latter approach can be strongly impaired by the heterogeneous spatiotemporal coverage and by the inequal quality of the individual data sets.

Whether the amplitude of PSV correlates with the reversal frequency remains a controversial issue. Numerical dynamo simulations predict an increase in PSV when more frequent polarity reversals occur (e.g., Lhuillier & Gilder, 2013). Nevertheless, this prediction cannot be directly applied to the Earth's dynamo because of (a) the excessive viscosity of the flow in such simulations, (b) the difficulty in modeling the process on geological timescales, and (c) the large uncertainties on the boundary conditions (e.g., Wicht & Sanchez, 2019). Over the past 200 Myr, paleomagnetic studies at high paleolatitude report lower PSV during the CNS than during the past 10 Myr (e.g., Lhuillier et al., 2024; Tarduno et al., 2002), consistent with the predictions from numerical dynamo simulations. Conversely, recent studies of the latitudinal dependency of PSV fail to identify a clear correlation with reversal frequency (e.g., Doubrovine et al., 2019; Engbers et al., 2024). Over the past 30 Myr, Lhuillier and Gilder (2019) reported an apparent decoupling between S_B and reversal frequency in the Afro-Arabian region, with S_B approximately 50% higher during the early Oligocene (reversal rate of 1.6 Myr^{-1}) than during the Plio-Pleistocene (reversal rate of 4.9 Myr^{-1}). Based on a compilation of 44 data sets for the Miocene (5.3–23 Ma), Engbers et al. (2022) reported an equatorial value of S_B approximately 20% higher during the Miocene (reversal rate of 4.6 Myr^{-1}) than during the past 10 Myr (reversal rate of 4.8 Myr^{-1}). In this compilation, 93% of the data sets yield a paleolatitude $|\lambda| < 50^\circ$; 86% (55%) of the data sets rely on less than 50 (25) independent directions. It indicates that the analysis at fixed paleolatitude is currently more realistic than the parameterization of latitudinal profiles. At the same time, larger data sets with more than 50 independent geomagnetic records are crucially needed to increase the precision of the S_B estimates.

The German Vogelsberg is the largest volcanic province in Central Europe, consisting of a few hundreds of eruption centers emplaced during the Early Middle Miocene (e.g., Reischmann & Schraft, 2010). The seminal paleomagnetic investigations of this area were conducted in the late 1950s on oriented block samples from quarries, to determine the pole of Central Europe (Angenheister, 1956; Nairn, 1960). Magnetostratigraphic investigations were later conducted on deep drilling cores, to better constrain the volcanic history of the area (Angenheister & Turkowsky, 1964; Ehrenberg et al., 1981; Harre et al., 1975; Schnepf et al., 2001). On the grounds that the paleomagnetic techniques had significantly evolved since the late 1950s, Sherwood (1990) undertook a new paleodirectional study on 1-inch core samples from 37 sites using stepwise alternating field (AF) demagnetization. However, with only three samples per cooling unit, no thermal (TH) demagnetization conducted on pilot samples, and less than 50 investigated cooling units, this study does not fulfill the modern paleomagnetic standards. In order to provide a robust estimate of PSV at mid-latitude during the Early Middle Miocene, we present in this paper a comprehensive paleomagnetic investigation of Vogelsberg, which quadruples the number of sampled sites, with on average 10 cores per site. Sections 2 and 3 introduce the geological background and the experimental methods. Section 4 describes the obtained results. Section 5 finally provides a discussion on the robustness of the data set and on the evolution of PSV during the 200 Myr at mid latitude.

2. Geological Settings

Located to the east of the Rhenish Massif between the Lower Rhine and Hesse grabens, the Vogelsberg is part of the Central European Volcanic Province stretching from the Massif Central to the Bohemian Massif (e.g., Hofbauer, 2021; Reischmann & Schraft, 2010). Covering a circular area of $\sim 2,500 \text{ km}^2$ and $\sim 60 \text{ km}$ diameter in the center of the state of Hesse (Germany), it was considered in the past as a shield volcano caused by a mantle plume (e.g., Ritter et al., 2001). Nowadays, it is interpreted as the piling of lavas from a few hundred of eruption

points, the activity of which is associated with extensional tectonics in the Alpine Foreland (e.g., Bourgeois et al., 2007; Lustrino & Carminati, 2007). Volcanism in the Vogelsberg started between ~18 and ~16 Ma with an alkali bimodal phase, intermittently interrupted by tholeiitic flows (e.g., Bogaard & Wörner, 2003; Nesbor, 2018). The alkali bimodal phase, typical for areas of extensional tectonics, consists of a complete sequence from ultramafic (basanite) to mafic (basalt) to felsic (trachyte) lavas. Volcanism in the Vogelsberg ended between ~16 and ~14 Ma, with a primitive phase dominated by basanitic and alkali basaltic lava flows.

Historically, ^{40}K - ^{40}Ar determinations were first conducted on outcropping rocks in the center and west of the Vogelsberg, yielding ages between ~19 and 15 Ma (Harre et al., 1975; Kreuzer et al., 1973; Lippolt et al., 1974; Turk et al., 1984). Nine ^{40}K - ^{40}Ar ages were also determined on the 300-m-deep drill core “Rainrod I” (50.474585°N, 9.086019°E, 195.5 m), defining a stratigraphy between ~17 and ~15 Ma except for two younger ages interpreted as shallow intrusions (Kreuzer et al., 1974). The 200-m-deep core “Flösser-Schneise” (50.509487°N, 9.254828°E, 652.1 m) and 490 m-deep core “Hasselborn” (50.525400°N, 9.292426°E, 559.5 m) gave further stratigraphic constraints, with the oldest age found at 18.2 ± 0.3 Ma (Ehrenberg et al., 1981). State-of-the-art ^{40}Ar - ^{39}Ar determinations and magnetostratigraphy of the 656-m-deep core “Vogelsberg 1996” (50.555850°N, 9.222341°E, 670 m) finally pointed to an emplacement of the lavas between 17.6 and 15.2 Ma (Bogaard et al., 2001; Schnepf et al., 2001). Based on one U-Pb, 8 ^{40}Ar - ^{39}Ar and 49 ^{40}K - ^{40}Ar age determinations, the last ones being recalculated using the K decay constants of Min et al. (2000) and the K abundance isotopic values of Böhlke et al. (2005), we obtained a distribution of ages between 14.0 and 18.7 Ma (95% confidence interval; Figure S1 in Supporting Information S1, Table S1), with a median of 16.4 Ma. However, given the inequal spatiotemporal distribution and heterogeneous quality of the ^{40}K - ^{40}Ar determinations, we rather rely on the range 15.2–17.6 Ma in the rest of this paper.

3. Method

3.1. Paleomagnetic Sampling

From 2021 to 2023, we sampled 162 paleomagnetic sites in the Vogelsberg (Figure 1). We identified the location of the sites thanks to the documentation from the Hessian Agency for Nature Conservation, Environment and Geology (Reischmann & Schraft, 2010), the previous paleomagnetic investigation by Sherwood (1990), as well as our own field observations. As reported in Figure 1 and Table S2, we sampled 42 sites from 12 active quarries (Figures 2a–2c), 52 sites from 37 previous quarries (Figures 2d–2g), 54 sites from natural outcrops (Figures 2h–2k), and 14 sites from road cuts (Figures 2l–2o), one locality consisting sometimes of several paleomagnetic sites (i.e., seemingly distinct cooling units). All the volcanic units were subhorizontal and we did not apply any stratigraphic correction to the paleomagnetic measurements.

At each site, we collected 8–12 paleomagnetic cores of 1-inch diameter and 6–8 cm length using a gasoline-powered drill, for a total of 1920 cores. Whenever possible, we preferably drilled in the bottom part of the cooling units to avoid overprints from the overlying unit, with samples ideally collected on different blocks and laterally spread over 2–20 m to average out the within-unit variability. We oriented the paleomagnetic cores using a Pomeroy fixture equipped with a sun compass and a Brunton magnetic compass. We successfully measured sun readings for 95% of the cores, which sometimes included returning to the relevant outcrops on the following days. After correcting the magnetic azimuths for the declination $D = 3.3^\circ$, calculated for the center of Vogelsberg (50.52°N, 9.20°E, 359 m) on 01.01.2022 using the 13th International Geomagnetic Reference Field model (Alken et al., 2021), we obtained an average magnetic anomaly of 0.3° (standard deviation of 8.0°). The absolute value of this anomaly is lower than 5° (10°) in 75% (85%) of the cases (Figure S2d in Supporting Information S1).

To conduct various rock-magnetic and demagnetization experiments at the Ludwig-Maximilians-Universität München (LMU, Germany), we first cut from the inner part of each paleomagnetic core a 1-cm high slice, then drilled an 8.8-mm diameter core in the center of this slice. The hollow slice of 1-inch diameter, termed A-specimen, was used for AF demagnetization, whereas the 8.8-mm diameter core, termed B-specimen, was used for TH demagnetization. After the AF demagnetization was completed, we drilled one to several 5-mm diameter cores from the A-specimen to conduct rock-magnetic experiments.

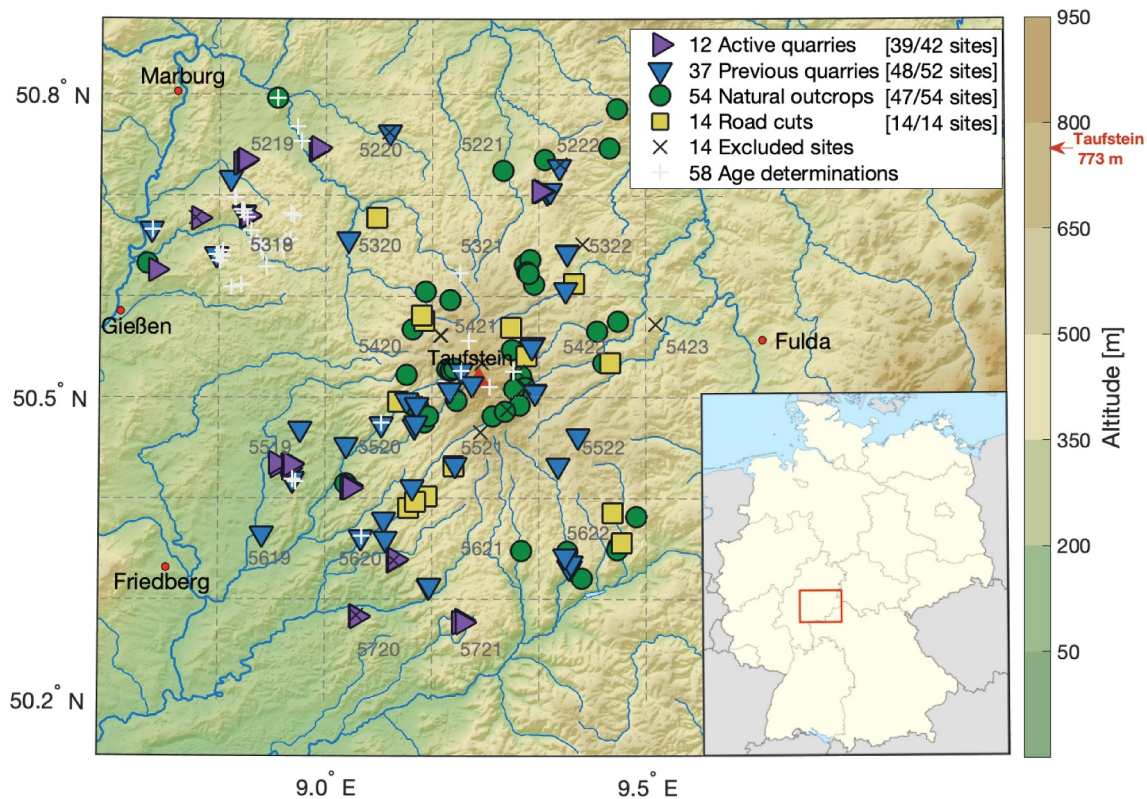


Figure 1. Topographic map of the Vogelsberg (adapted from [https://commons.wikimedia.org/wiki/File:Vogelsberg_\(Relief_und_Gew%C3%A4sser\)_-_Deutsche_Mittelgebirge,_Serie_A-de.png](https://commons.wikimedia.org/wiki/File:Vogelsberg_(Relief_und_Gew%C3%A4sser)_-_Deutsche_Mittelgebirge,_Serie_A-de.png)), with the inset showing the location of the area in Germany (adapted from https://commons.wikimedia.org/wiki/File:Germany_location_map.svg). The purple right-pointing triangles (active quarries), blue down-pointing triangles (previous quarries), green circles (natural outcrops) and yellow squares (road cuts) represent the localities investigated in this study, with the number of interpreted sites/sampled sites being provided in the legend of the figure. The black x-marks indicate the paleomagnetic sites that could not be interpreted; the gray plus symbols the location of the radio-isotopic determinations (see Table S1). The gray dashed lines show the limits of the 1:25,000 topographic map (TK25, gray number). Taufstein corresponds to the highest point (773 m) in the Vogelsberg.

3.2. Rock-Magnetic Experiments

We conducted rock-magnetic experiments on 1–3 samples per paleomagnetic site, ideally coming from different sampling blocks to better assess the within-unit variability. Hysteresis loops and backfield curves of the isothermal remanent magnetization (IRM) were measured using a Lake Shore Vibrating Sample Magnetometer (VSM). The bulk rock-magnetic properties—saturation magnetization (M_S), remanent saturation magnetization (M_{RS}), coercive force (B_C), and remanent coercive force (B_{CR})—were determined after the correction of the hysteresis loop for the paramagnetic contribution by the slope above 0.8 T. These properties were analyzed in the Néel diagram (Néel, 1955) to be compared with the reference curves of magnetite and TM60 (Wang & Van der Voo, 2004), where TM60 stands for titanomagnetite $Fe_{3-x}Ti_xO_4$ with ulvöspinel content x of 0.6. For comprehensiveness, the properties were also analyzed in the Day diagram (Day et al., 1977) to be compared with the reference curves for the mixture of single domain (SD) and multidomain (MD) grains of magnetite (Dunlop, 2002).

Continuous thermomagnetic curves $M_S(T)$ were measured using a homemade Variable Field Translation Balance (VFTB) by heating the samples up to 620°C and cooling them down to room temperature in the air under a field of ~300 mT. The Curie points T_C of the ferrimagnetic phases were associated with the minima of the first derivative of the heating branches of the $M_S(T)$ curves (e.g., Fabian et al., 2013). To better assess the thermostability of 80 representative samples, cyclic $M_S(T)$ curves were finally measured with peak temperatures of 200°C, 300°C, 400°C, 500°C and 600°C, again in an ambient field of ~300 mT.



Figure 2. Field photographs of representative sites sampled from active quarries (a–c), previous quarries (d–g), natural outcrops (h–k), and road cuts (l–o).

3.3. Paleomagnetic Experiments

Before starting the demagnetization experiments, we measured the magnetic susceptibility χ_m of each sample using a Bartington MS2B dual frequency susceptibility meter operated in the LF mode (0.4565 kHz). We then computed the Q-ratio of the natural remanent magnetization (NRM) to the induced magnetization $\chi_m \cdot B/\mu_0$ (Koenigsberger, 1938), where $B = 49.2$ mT is the reference field in the center of Vogelsberg (50.52°N, 9.20°E, 359 m) on 01.01.2024 derived from the 13th International Geomagnetic Reference Field model (Alken et al., 2021).

We carried out all demagnetization experiments in a 30 m² magnetically shielded room at LMU, characterized by a residual field lower than $\sim 1,000$ nT. Progressive AF demagnetization of the A-specimens were conducted in 14–17 steps using the homemade SushiBar system, which automates the remanence measurements (with a 2G Enterprises, three-axis, superconducting magnetometer) and the demagnetization (with a custom-made coil reaching a peak field of 90 mT) for a batch of 99 samples (Wack & Gilder, 2012). If needed, the A-specimens were further demagnetized up to 200 mT using an ASC D2000 coil. For comparison, progressive thermal demagnetization experiments were conducted on 1–3 B-specimens for each paleomagnetic site in 12–17 steps up to 600°C using an AGICO JR6 spinner magnetometer and an ASC TD-48 dual-chamber furnace. The demagnetization results were visualized using vector endpoint diagrams (Zijderveld, 1967), the individual ChRM directions being isolated by principal component analysis (PCA; Kirschvink, 1980) with the aid of paleomagnetism.org (Koymans et al., 2016, 2020).

3.4. Statistical Analysis

We analyzed the site distributions using Fisher (1953)'s statistics, wherein the precision parameter k (the 95% confidence radius α_{95}) describes the dispersion of the distribution (the uncertainty on the mean direction). We used the elongation parameter e from Tauxe (1998) to quantify the geometry of the distributions. We checked the existence of directional correlations between successive or adjacent flows using (a) the statistical test by Chenet et al. (2008) based on the comparison of the angular distance with the quadratic sum of the corresponding α_{95} values; and (b) the conventional test for a common mean by Watson (1983) assuming that the distributions are Fisherian. We combined the correlated directions into directional groups (DGs) assuming that they represent geomagnetic snapshots (e.g., Lhuillier & Gilder, 2019). We detected transitional directions using a fixed 45° (McElhinny & McFadden, 1997) or adaptive VGP cutoff (Vandamme, 1994). Finally, we tested the antipodality of the populations of normal and reversed polarity using (a) Watson (1983)'s test along with the classification by McFadden and McElhinny (1990); and (b) the bootstrap test for a common mean by Heslop et al. (2023).

We computed the VGP scatter, corrected for within-flow dispersion, using the formula

$$S_B = \sqrt{\frac{1}{N-1} \sum_{i=1}^n \left(\Delta_i^2 - \frac{S_{wi}^2}{n_i} \right)}, \quad (1)$$

where Δ_i denotes the angular distance between the VGP of the i^{th} flow and the mean paleomagnetic pole of the whole collection (Cox, 1970); S_{wi} is the angular standard deviation of the n_i individual VGPs from the i^{th} flow; N is the number of flows (McElhinny & McFadden, 1997). The 95% uncertainty on S_B was calculated by bootstrapping 100,000 pseudo sets of VGPs from the original collection of VGPs (e.g., Tauxe et al., 1991).

4. Results

4.1. Rock-Magnetic Results

We identified four different groups based on the bulk hysteresis and thermomagnetic properties of the samples (Figure 3). Samples from group 1 (35 out of 148 sites) closely follow the reference curve for TM60 in the Néel diagram, consistent with the observed T_C between 56 and 170°C (interquartile range; Figure 3b and Figure S2f in Supporting Information S1). The thermomagnetic behavior is reversible below T_C , whereas ongoing oxidation during the experiments leads to an approximately twofold increase in M_S (Figure 3c). Samples from group 4 (33 out of 148 sites) closely follow the reference curve for magnetite in the Néel diagram, consistent with the observed T_C between 516 and 548°C (interquartile range; Figure 3i and Figure S2f in Supporting Information S1). These samples are thermally stable until 600°C (Figure 3j). Between these two textbook cases, samples from group 2 (48 out of 148 sites) are characterized by the coexistence of at least two T_C (Figure 3d). The dominant T_C is generally close to the one of group 1, consistent with the location of the points in the Néel diagram. These samples show higher thermostability than those from group 1 (Figure 3e), indicating that titanomagnetite from group 2 are more oxidized (and titanium depleted) than those from group 1. Finally, samples from group 3 (32 out of 148 sites) are characterized by a single T_C between 498 and 511°C (Figure 3g and Figure S2f in Supporting Information S1), close to the one from group 4. However, they lie slightly above the reference curve for magnetite in the Néel diagram. They are also more prone to rock-magnetic transformations in the course of the experiments, leading to a slight decrease in M_S (Figure 3h).

4.2. Demagnetization Results

Among the 340 pairs of sister specimens simultaneously demagnetized by AF and TH treatment (see examples in Figures 4 and 5), we successfully interpreted the AF and TH demagnetization spectra of 302 pairs (150 out of 162 sites). Because of lightning-induced IRM (LIRM) overprints, we failed to interpret the TH demagnetization spectra, but successfully interpreted the AF demagnetization spectra, from 6 sites (see example in Figure 4b). Four of these sites (sites 17, 35, 120 and 136) belong to rock-magnetic group 1; two of them (sites 57 and 82) belong to group 2. Additionally, we failed to interpret both AF and TH demagnetization spectra from 14 sites because of LIRM overprints and/or erratic demagnetization behavior (see examples in Figure S3 in Supporting Information S1). For the 302 pilot samples successfully interpreted, the median destructive field (MDF) lies in the interquartile range 14–37 mT, with a median value gradually increasing from 18 mT for rock-magnetic group 1, to

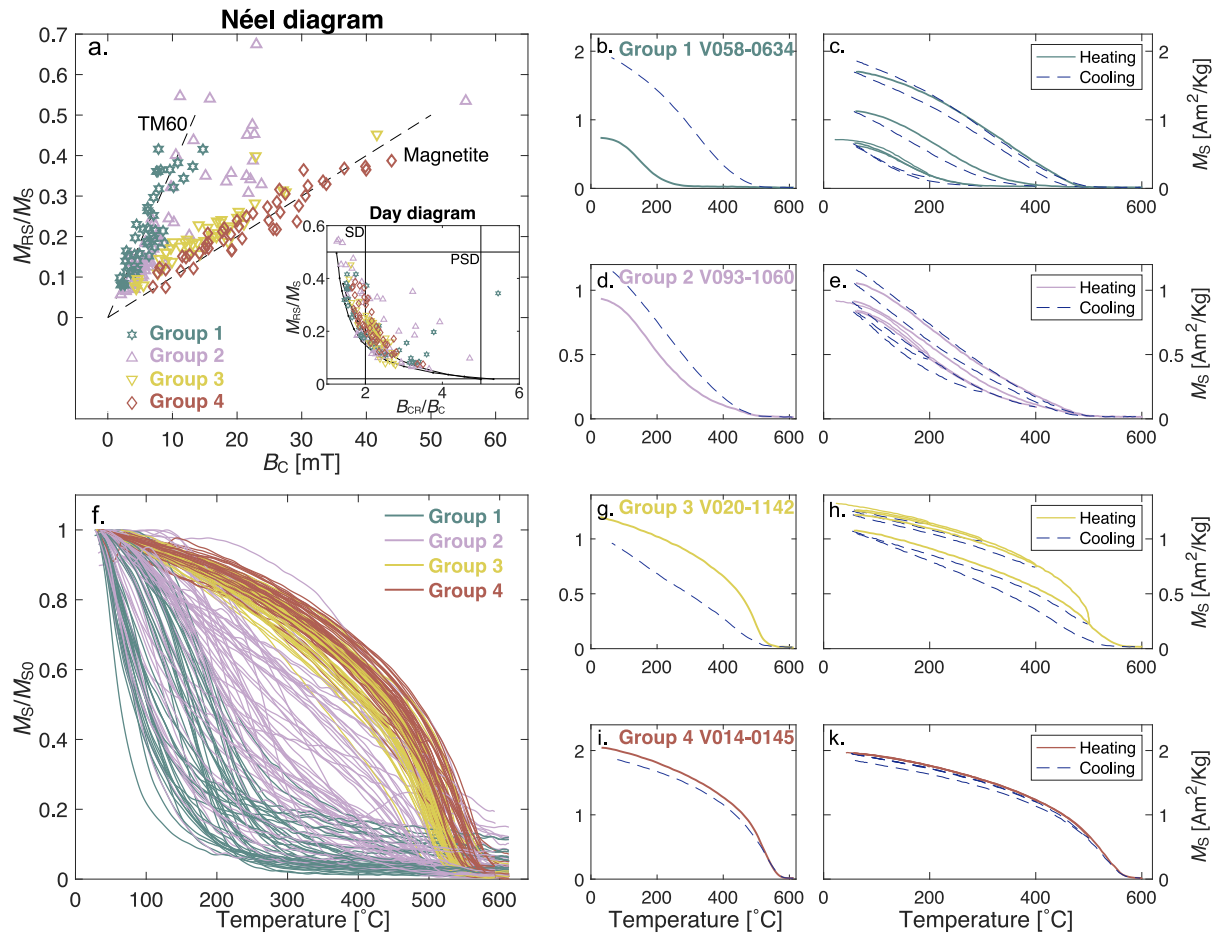


Figure 3. Rock-magnetic properties of representative samples. (a) Néel diagram showing the reference curves of magnetite and titanomagnetite with 60% titanium content (TM60) by Wang and Van der Voo (2004). Day diagram in the inset showing the single domain/multidomain mixing curves of magnetite by Dunlop (2002). (b, d, g, i) Heating and cooling (blue dashed line) branches of $M_S(T)$ curves for representative samples from the four rock-magnetic groups defined in Section 4.1. (c, e, h, j) Heating and cooling (blue dashed line) branches of cyclic $M_S(T)$ curves for the same representative samples. (f) Stack of the heating branches of the $M_S(T)$ curves for the whole collection of samples.

24 mT for group 2, to 29 mT for group 3, to 30 mT for group 4. The 95% unblocking temperature T_U lies in the interquartile range 480–548°C, with a median value gradually increasing from 455°C for group 1, to 511°C for group 2, to 528°C for group 3, to 550°C for group 4. Consequently, the increase, from group 1 to 4, in the coercivity of the remanence carriers observed in the demagnetization spectra directly correlates with the decrease, from group 1 to 4, in the ulvöspinel content of the titanomagnetite grains revealed by the rock-magnetic experiments (Section 4.1).

For the 302 pilot samples successfully interpreted, the secondary component of magnetization is removed by 10–25 mT (interquartile range) for AF demagnetization, independently of the rock-magnetic group. This secondary component is removed by 150–350°C (interquartile range) for TH demagnetization, with a median value increasing from 150°C for group 1, to 225°C for group 2, to 250°C for group 3, to 300°C for group 4. At higher coercivity, the ChRM component uniaxially decays toward the origin in the vector endpoint diagrams, with the angle α between the origin-anchored and free-floating PCA directions lying in the interquartile range 0.6–2.3° for AF demagnetization, 0.7–4.2° for TH demagnetization. The PCA fits are well constrained, with the maximum angular deviation (MAD) lying in the interquartile range 0.5–1.3° for AF demagnetization, 1.5–4.1° for TH demagnetization. Generally, the median MAD values are 2–5 times higher for TH demagnetization than for AF demagnetization, the smallest values being observed for rock-magnetic group 4. The PCA directions show reasonable agreement between the pairs of sister specimens demagnetized by AF and TH treatment, with the angular distance lower than 5° in 50% of the cases, and lower than 10° in 84% of the cases. Among the five sites

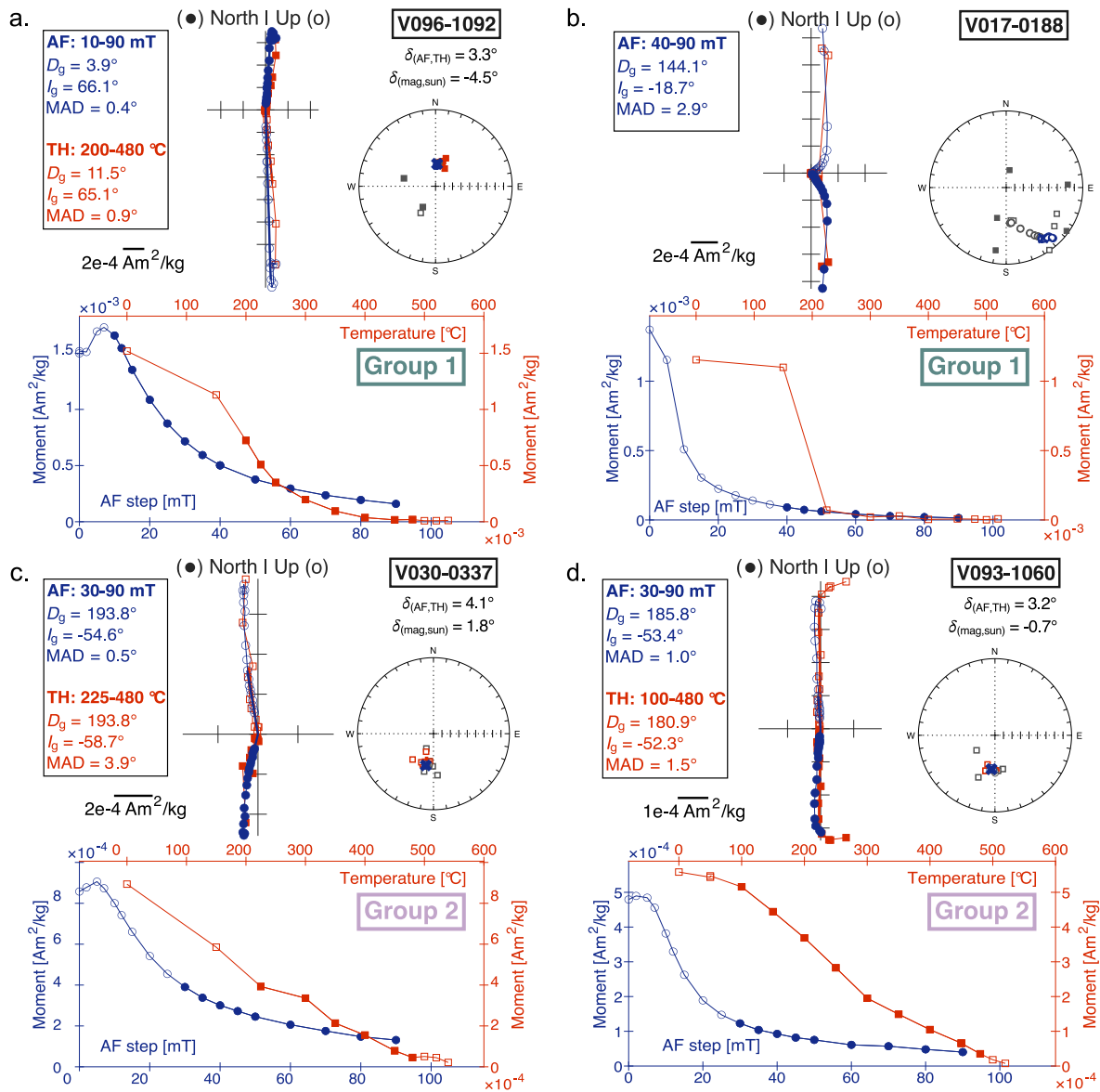


Figure 4. Vector endpoint diagrams, stereographic projections, and demagnetization spectra for two representative samples from rock-magnetic groups 1 and 2. The demagnetization behaviors by alternating field (AF) and thermal (TH) treatment are represented by blue circles and red squares, respectively. The anchored direction (D_g , I_g) in geographic coordinates determined by principal component analysis (PCA), the maximum angular deviation MAD, the angular distance $\delta_{(AF,TH)}$ between each pair of directions obtained by AF and TH treatment, and the magnetic anomaly $\delta_{(mag,sun)}$ (if a sun reading was available) are provided in the insets. The crosses on the stereographic projections correspond to the PCA fits; the gray symbols correspond to the points excluded from the PCA fits.

with the average $\delta > 10^\circ$, four of them (sites 26, 32, 36 and 81) belong to rock-magnetic group 2; one of them (site 12) belongs to group 3.

As a consequence, due to the better efficacy of AF demagnetization (especially in the case of samples with LIRM overprints and/or low unblocking temperatures) and the better precision of automated AF demagnetization, we chose to AF demagnetize the rest of the collection. For a total of 1,878 samples from 162 sites, the NRM intensity (resp. the Q-ratio) lies in the interquartile range 1.2–4.2 A/m (resp. 1.4–8.1), with both quantities being in first approximation independent of the rock-magnetic groups (Table S2). We successfully interpreted 1784 AF demagnetization curves from 148 sites, with a median of 10 interpreted samples (interquartile range of 8–11) per site (Table 1). Similarly to the behavior observed for the pilot samples, we isolated the ChRM component by PCA from 10–25 mT to 80–90 mT (interquartile ranges). The fitted components are well constrained—with the MAD

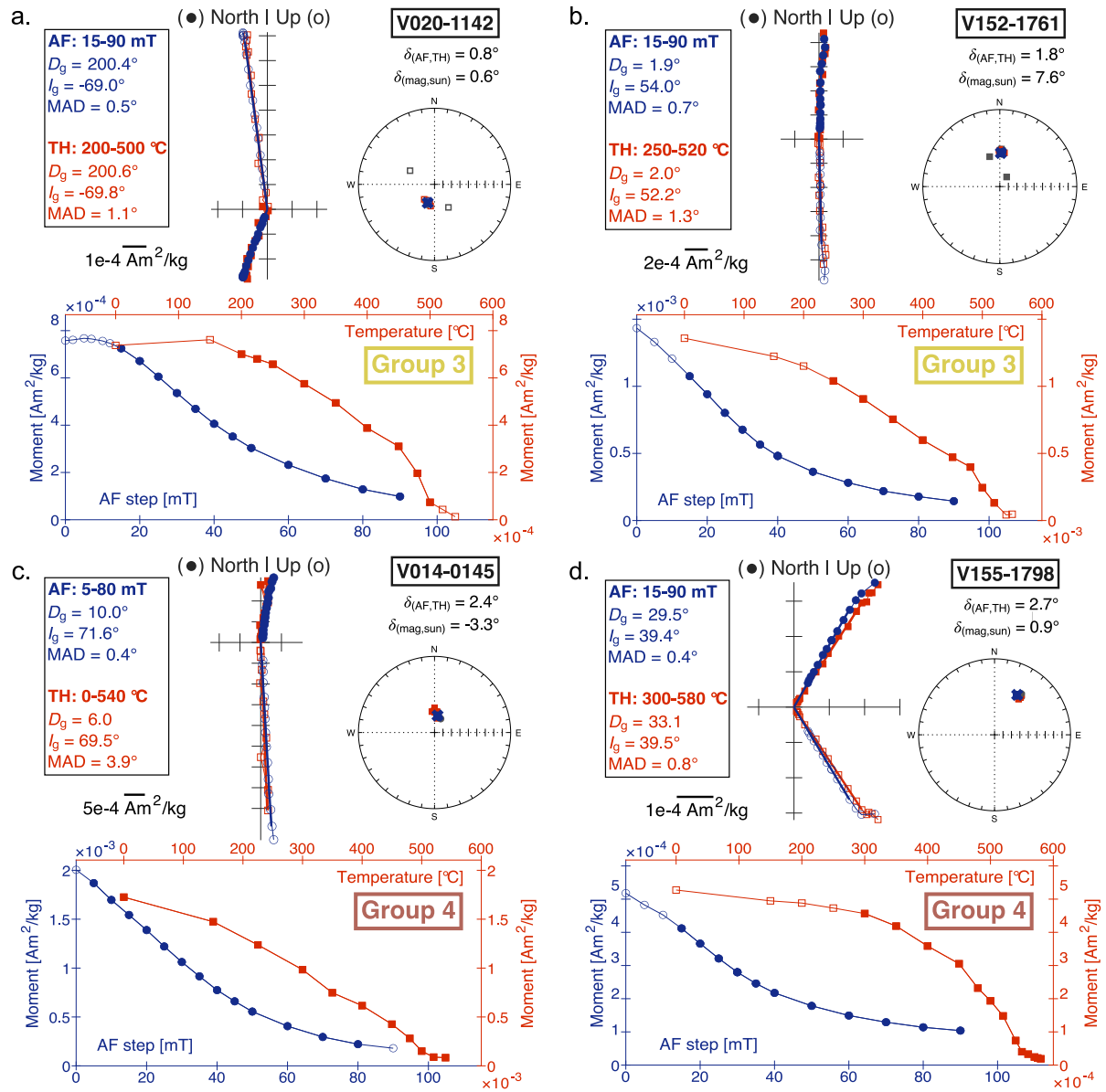


Figure 5. Vector endpoint diagrams, stereographic projections, and demagnetization spectra for two representative samples from rock-magnetic groups 3 and 4. The insets provide the same information as in Figure 4.

lying in the interquartile range 0.6–1.6°—and uniaxially decay toward the origin—with the parameter α lying in the interquartile range 0.6–2.7°. We again excluded 14 sites from the analysis due to strong LIRM overprints and/or erratic demagnetization behavior (Figure S3 in Supporting Information S1).

4.3. Paleodirectional Results

The Fisher statistics of the 148 interpreted sites are provided in Table 1. In terms of dispersion of the site distributions, the k parameter lies in the interquartile range 220–484 (median of 318), and exceeds 100 (50) in 95% (98%) of the cases. In terms of confidence of the site-mean directions, the α_{95} angle lies in the interquartile range 2.2–3.6° (median of 2.7°), and is lower than 5° (10°) in 93% (100%) of the cases. Among the 148 interpreted sites, we detected 9 transitional sites with a fixed VGP cutoff ($A = 45^\circ$) and 13 transitional directions with an adaptive VGP cutoff ($A = 39.2^\circ$). Considering the case of an adaptive VGP cutoff, we obtained 63 (72) directions of normal (reversed) polarity (Table 2; Figures 6a–6c). The reversal test is positive (classification A of McFadden & McElhinny, 1990), with the angle $\theta = 2.0^\circ$ between the populations of normal and reversed polarity not

Table 1
Paleomagnetic Results of the 148 Sites Interpreted in This Study

Site	Locality	Slon	Slat	Salt	<i>n</i>	<i>N</i>	<i>D_g</i>	<i>I_g</i>	<i>k</i>	<i>α₉₅</i>	Plon _g	Plat _g	<i>S_w</i>
66	Nieder-Ofleiden	8.98	50.74	279	11	13	178.0	-48.3	256.5	2.9	13.7	-68.6	5.6
67	Nieder-Ofleiden	8.99	50.75	292	11	12	166.8	-57.3	134.9	3.9	51.5	-74.2	9.3
10	Dreihausen	8.85	50.72	310	8	8	339.8	68.7	172.4	4.2	293.8	77.5	10.0
90	Amöneburg	8.92	50.80	318	9	10	11.3	67.7	555.8	2.2	94.5	82.9	5.1
52	Dreihausen ^c	8.87	50.73	295	9	11	220.2	-23.1	103.7	5.1	314.0	-39.4	7.0
50	Dreihausen	8.87	50.73	324	11	11	203.5	-53.4	118.5	4.2	313.8	-66.3	8.8
51	Dreihausen	8.87	50.73	365	7	9	210.6	-62.4	393.1	3.0	285.7	-68.3	6.3
136	Kirtorf ^c	9.10	50.76	305	10	10	352.8	3.1	30.8	8.8	198.4	40.4	10.9
11	Altenburg	9.28	50.72	330	17	21	4.5	60.2	319.3	2.0	169.3	80.1	5.8
123	Brauerschwend	9.33	50.70	309	10	10	358.0	60.0	208.8	3.4	198.9	80.2	7.8
46	Brauerschwend	9.34	50.70	334	10	10	348.2	60.4	285.2	2.9	235.5	77.6	6.8
122	Brauerschwend	9.33	50.70	343	10	11	2.6	52.8	649.5	1.9	181.8	72.6	4.1
47	Brauerschwend	9.33	50.70	368	9	11	2.3	38.1	175.3	3.9	184.8	60.8	6.1
48	Brauerschwend	9.34	50.70	407	8	8	155.4	-59.5	200.0	3.9	78.4	-70.2	7.3
8	Brauerschwend	9.35	50.70	424	10	10	159.1	-73.4	348.5	2.6	143.4	-75.3	7.4
124	Brauerschwend	9.35	50.70	430	10	10	164.9	-68.4	890.9	1.6	110.9	-80.5	4.1
7	Eifa ^c	9.36	50.73	375	12	15	232.3	72.3	41.2	6.8	341.5	26.8	20.5
126	Eifa	9.34	50.73	396	9	9	18.2	45.7	380.2	2.6	152.1	62.8	4.3
150	Grebenau	9.44	50.75	358	8	9	30.5	58.7	218.6	3.8	115.2	66.1	7.3
149	Grebenau	9.45	50.79	396	8	9	357.1	50.1	200.0	3.9	197.0	70.1	6.3
54	Staufenberg	8.73	50.67	230	8	10	161.5	-48.2	277.4	3.3	48.7	-64.5	6.0
141	Alten-Buseck	8.72	50.63	237	10	10	191.0	-59.4	506.2	2.1	328.0	-77.2	4.6
83	Alten-Buseck	8.73	50.62	260	6	6	188.8	-51.8	227.8	4.4	345.6	-71.0	5.3
69	Allendorf	8.80	50.68	232	11	11	187.4	-71.8	166.7	3.5	221.1	-82.5	10.6
13	Beuern	8.83	50.64	250	11	12	163.1	-66.1	343.5	2.5	95.0	-78.9	6.6
87	Londorf	8.88	50.68	285	11	11	34.3	67.5	374.4	2.4	85.8	68.5	6.4
88	Londorf	8.88	50.68	299	10	12	30.5	72.2	1,647.3	1.2	66.6	71.1	3.4
84	Londorf	8.88	50.68	301	10	12	32.8	67.6	2,311.4	1.0	86.6	69.4	2.6
140	Londorf	8.87	50.68	307	11	11	27.1	63.9	586.4	1.9	104.0	71.4	4.9
86	Londorf ^{da}	8.87	50.68	311	8	11	31.1	69.9	802.9	2.0	77.4	70.9	4.6
68	Londorf ^{da}	8.87	50.68	316	10	10	26.0	72.4	481.4	2.2	63.8	73.4	6.1
85	Londorf ^{da}	8.87	50.68	317	11	12	34.9	70.6	286.9	2.7	73.3	68.9	7.5
139	Londorf ^{da}	8.87	50.68	318	8	9	28.2	70.9	786.3	2.0	72.5	72.5	4.7
138	Londorf ^{da}	8.87	50.68	319	10	10	31.5	68.4	335.5	2.6	83.3	70.5	6.7
170	<i>DG01</i> (V068 + 085 + 086 + 138 + 139)			316	47	52	30.6	70.5	388.3	1.1	74.3	71.3	6.5
89	Londorf	8.88	50.68	325	11	11	4.9	29.8	372.4	2.4	180.6	55.2	2.8
71	Elpenrod	9.08	50.68	262	10	14	174.3	-55.9	325.9	2.7	27.2	-75.4	5.1
70	Nieder-Ohmen	9.03	50.66	267	10	10	18.7	48.6	351.1	2.6	148.4	64.8	5.1
14	Unter-Seibertenrod	9.15	50.60	440	13	20	14.5	72.0	493.3	1.9	56.3	79.2	5.9
63	Allmenrod	9.31	50.63	419	10	10	173.1	-65.1	175.0	3.7	67.1	-84.3	9.1
64	Allmenrod ^{da}	9.32	50.64	420	8	11	357.8	58.8	222.6	3.7	198.4	79.0	6.6
152	Allmenrod ^{da}	9.32	50.61	438	11	11	354.3	57.3	688.0	1.7	209.5	76.8	3.8

Table 1
Continued

Site	Locality	Slon	Slat	Salt	<i>n</i>	<i>N</i>	<i>D_g</i>	<i>I_g</i>	<i>k</i>	α_{95}	Plon _g	Plat _g	<i>S_w</i>
12	Allmenrod ^a	9.31	50.62	448	13	20	358.5	59.8	486.0	1.9	196.2	80.1	4.7
171	DG02 (V012 + 064 + 152)			435	32	42	356.8	58.7	381.9	1.3	202.1	78.8	5.2
151	Allmenrod	9.32	50.62	456	10	10	352.9	54.8	257.1	3.0	211.0	74.0	6.1
43	Lauterbach	9.38	50.64	347	10	10	348.8	54.3	323.2	2.7	221.0	72.4	5.2
44	Lauterbach	9.38	50.64	356	9	9	358.3	56.2	609.3	2.1	195.2	76.2	3.5
121	Fischborn ^c	9.39	50.61	362	7	10	260.8	-51.2	120.7	5.5	264.0	-29.9	8.3
9	Fischborn	9.37	50.61	420	10	10	160.5	-62.4	602.8	2.0	79.3	-75.1	5.0
148	Bobenhausen II	9.15	50.58	410	8	10	169.0	-68.1	201.2	3.9	110.6	-83.2	9.0
130	Bobenhausen II	9.15	50.58	420	10	10	339.0	68.6	309.2	2.8	294.4	76.9	7.0
129	Bobenhausen II	9.13	50.57	457	11	11	356.6	51.5	562.3	1.9	198.3	71.5	4.2
145	Betzenrod	9.13	50.52	468	11	12	346.5	63.6	338.7	2.5	254.3	79.7	6.1
55	Feldatal	9.19	50.60	555	8	9	353.3	65.6	370.3	2.9	251.0	84.9	5.8
142	Breungeshain	9.19	50.51	545	10	13	212.3	-35.1	426.8	2.3	317.9	-49.8	3.6
82	Rudingshain	9.19	50.53	554	9	11	152.4	-64.2	128.8	4.6	96.6	-71.6	10.1
61	Rudingshain	9.19	50.53	587	9	12	165.4	-65.6	642.0	2.0	89.5	-80.2	4.7
60	Rudingshain ^a	9.20	50.53	601	21	24	184.2	-60.6	290.5	1.9	349.1	-80.7	6.8
78	Rudingshain ^a	9.20	50.53	605	7	11	184.0	-58.8	282.2	3.6	352.5	-78.8	6.3
172	DG03 (V060 + 078)			603	28	35	184.2	-60.2	291.3	1.6	350.1	-80.2	6.6
33	Rudingshain	9.21	50.53	650	22	23	210.0	-41.1	283.4	1.8	317.3	-54.5	4.3
169	Hoherodskopf	9.23	50.51	738	11	11	174.2	-66.2	222.5	3.1	80.2	-85.8	7.4
62	Lanzenhain	9.32	50.55	436	11	11	358.6	63.4	254.8	2.9	199.7	84.4	7.8
110	Lanzenhain	9.32	50.55	474	9	12	356.7	53.6	43.1	7.9	195.9	74.5	14.6
27	Lanzenhain ^a	9.31	50.54	497	9	10	2.6	62.2	197.9	3.7	171.8	82.8	8.2
154	Lanzenhain ^a	9.31	50.54	532	11	11	0.2	65.6	591.8	1.9	186.5	87.3	4.6
173	DG04 (V027 + 154)			515	20	21	1.4	64.1	284.7	1.9	176.4	85.3	6.7
153	Lanzenhain	9.29	50.57	550	10	10	195.1	-61.2	1,125.2	1.4	311.8	-76.8	3.3
155	Lanzenhain	9.29	50.55	571	10	10	26.8	40.7	1,061.0	1.5	141.9	55.7	2.3
25	Ilbeshausen	9.33	50.51	530	12	12	315.9	81.5	275.6	2.6	345.8	60.4	9.3
107	Ilbeshausen ^b	9.33	50.50	535	15	15	292.7	72.4	295.5	2.2	316.9	51.6	7.8
158	Ilbeshausen	9.31	50.51	537	6	11	32.3	47.0	231.9	4.4	129.5	57.1	5.7
112	Ilbeshausen	9.30	50.52	542	6	12	36.4	58.6	229.9	4.4	108.9	62.5	7.1
26	Ilbeshausen	9.31	50.51	555	11	19	359.4	70.3	110.0	4.4	4.0	85.5	12.0
156	Ilbeshausen	9.29	50.51	588	9	11	5.5	41.7	318.3	2.9	177.9	63.3	4.2
57	Schadges ^a	9.42	50.56	363	5	8	182.3	-61.8	190.0	5.6	356.3	-82.5	7.6
65	Stockhausen ^a	9.46	50.57	445	6	11	175.9	-60.8	442.7	3.2	28.8	-80.9	5.2
174	DG05 (V057 + 065)			404	11	19	178.8	-61.3	273.2	2.8	15.7	-81.9	6.6
58	Schlechtenwegen	9.44	50.53	360	12	12	190.1	-55.0	295.6	2.5	339.4	-73.4	6.1
108	Schlechtenwegen	9.44	50.53	365	7	11	178.9	-59.4	503.1	2.7	14.0	-79.7	4.2
109	Schlechtenwegen	9.43	50.53	375	5	9	199.4	-56.6	236.4	5.0	315.4	-70.8	7.0
32	Langd	8.96	50.47	165	15	21	63.2	81.7	296.0	2.2	34.9	55.2	8.9
35	Widdersheim ^a	8.92	50.43	81	9	9	174.7	-32.9	78.0	5.9	18.0	-57.4	9.0
36	Widdersheim ^a	8.92	50.43	101	12	12	172.1	-36.7	116.0	4.0	23.7	-59.6	7.1
175	DG06 (V035 + 036)			91	21	21	173.2	-35.1	94.1	3.3	21.2	-58.7	7.9

Table 1
Continued

Site	Locality	Slon	Slat	Salt	<i>n</i>	<i>N</i>	<i>D_g</i>	<i>I_g</i>	<i>k</i>	α_{95}	Plon _g	Plat _g	<i>S_w</i>
41	Widdersheim	8.94	50.43	112	10	11	175.4	-63.7	430.2	2.3	43.0	-84.2	5.3
34	Widdersheim	8.92	50.43	125	9	10	171.7	-44.4	148.3	4.2	26.7	-65.1	6.0
40	Widdersheim	8.94	50.43	141	11	11	176.7	-60.4	363.7	2.4	24.5	-80.8	5.6
39	Widdersheim	8.94	50.43	170	13	13	2.5	79.2	214.9	2.8	11.7	70.9	10.2
38	Widdersheim	8.94	50.43	171	9	9	343.8	66.4	993.8	1.6	276.5	79.4	4.1
37	Widdersheim	8.94	50.43	181	6	8	357.9	65.5	250.5	4.2	218.8	86.9	7.9
99	Widdersheim ^a	8.95	50.42	175	10	10	312.2	-23.1	74.0	5.7	237.6	14.7	6.7
100	Widdersheim ^a	8.95	50.42	180	11	11	306.4	-21.6	197.3	3.3	243.0	12.7	3.7
176	<i>DG07</i> (V099 + 100) ^c			178	21	21	309.1	-22.3	101.8	3.2	240.4	13.7	5.9
98	Nidda ^a	9.03	50.41	160	8	10	1.4	68.1	519.3	2.4	50.1	88.7	5.4
97	Nidda ^a	9.03	50.41	175	8	9	3.4	66.7	363.1	2.9	121.3	87.6	6.5
96	Nidda ^a	9.03	50.41	180	9	10	6.2	67.1	467.9	2.4	103.7	86.1	5.7
177	<i>DG08</i> (V096 + 097 + 098)			172	25	29	3.8	67.3	449.6	1.4	101.3	87.6	5.8
91	Nidda	9.03	50.41	195	9	10	351.7	70.2	778.8	1.8	320.0	83.6	4.6
92	Nidda ^a	9.03	50.41	214	10	10	184.1	-57.8	233.0	3.2	353.6	-78.0	5.9
95	Nidda ^a	9.04	50.41	217	9	10	182.5	-59.4	354.4	2.7	358.5	-79.8	5.6
93	Nidda ^a	9.03	50.41	236	9	9	183.8	-59.0	262.7	3.2	353.2	-79.2	6.5
178	<i>DG09</i> (V092 + 093 + 095)			222	28	29	183.5	-58.7	286.4	1.6	354.9	-79.0	5.9
94	Nidda	9.04	50.41	245	9	10	349.8	60.4	482.9	2.3	231.2	78.6	4.8
42	Ober-Schmitten	9.03	50.45	210	10	10	156.1	-60.9	278.9	2.9	81.1	-71.6	7.1
81	Rainrod ^a	9.09	50.47	198	15	15	124.6	-68.1	225.7	2.6	122.6	-55.9	8.4
6	Rainrod ^a	9.09	50.47	214	7	10	129.0	-65.9	782.1	2.2	115.4	-57.4	4.3
179	<i>DG10</i> (V006 + 081)			206	22	25	126.1	-67.4	279.4	1.9	120.3	-56.4	7.5
146	Schotten	9.11	50.50	275	9	10	202.1	-76.2	554.4	2.2	221.9	-72.2	5.9
1	Schotten	9.13	50.50	300	18	23	183.2	-79.0	313.4	2.0	192.7	-71.5	8.3
3	Schotten ^a	9.15	50.47	340	6	9	220.8	-79.1	212.1	4.6	220.5	-63.3	10.4
168	Schotten ^a	9.14	50.49	350	10	12	236.8	-80.1	263.6	3.0	219.6	-57.6	9.2
180	<i>DG11</i> (V003 + 168)			345	16	21	230.4	-79.8	238.0	2.4	219.9	-59.7	9.7
134	Schotten	9.13	50.49	355	15	19	234.3	-75.3	120.9	3.5	235.3	-59.0	12.9
4	Schotten ^b	9.14	50.47	360	8	11	117.0	-63.9	182.4	4.1	117.9	-49.0	8.9
133	Schotten ^a	9.14	50.49	365	10	10	211.2	-74.7	1,018.8	1.5	235.0	-69.7	4.5
132	Schotten ^a	9.14	50.49	373	11	11	210.7	-76.4	318.4	2.6	226.9	-68.9	8.2
2	Schotten ^a	9.16	50.48	380	8	9	201.6	-75.8	230.5	3.7	222.7	-72.5	9.1
181	<i>DG12</i> (V002 + 132 + 133)			373	29	30	208.4	-75.7	360.4	1.4	228.7	-70.2	7.5
5	Schotten	9.14	50.47	390	9	10	129.4	-65.5	317.5	2.9	114.6	-57.4	6.8
159	Merkenfritz	9.16	50.40	280	10	10	159.7	-64.7	478.5	2.2	91.4	-76.1	5.4
80	Glashütten ^b	9.13	50.41	299	10	10	121.6	-64.9	208.4	3.4	117.7	-52.3	7.9
160	Gedern	9.20	50.43	340	9	10	195.4	-51.8	538.1	2.2	331.0	-68.8	4.0
79	Gedern	9.20	50.43	354	9	12	187.8	-15.2	203.8	3.6	357.9	-46.8	3.4
144	Busenborn	9.20	50.50	630	8	12	190.1	-62.2	1,292.4	1.5	320.9	-80.2	3.4
143	Busenborn	9.20	50.50	665	5	5	160.0	-75.7	271.2	4.7	155.7	-73.5	9.0
24	Herchenhain	9.30	50.49	540	11	11	351.3	55.9	318.7	2.6	216.9	74.8	5.5
22	Herchenhain	9.26	50.48	609	5	9	189.4	-44.9	560.3	3.2	348.8	-65.0	3.5

Table 1
Continued

Site	Locality	Slon	Slat	Salt	<i>n</i>	<i>N</i>	D_g	I_g	<i>k</i>	α_{95}	Plon _g	Plat _g	S_w
23	Herchenhain	9.28	50.49	710	8	10	17.1	51.2	261.0	3.4	148.4	67.7	5.3
20	Salz	9.36	50.43	430	20	20	195.4	-70.9	337.4	1.8	245.1	-79.5	7.2
59	Gunzenau	9.39	50.46	535	8	8	229.8	-73.8	338.3	3.0	240.9	-60.8	7.4
161	Bingenheim	8.90	50.36	135	19	21	187.6	-58.1	262.9	2.1	340.7	-77.4	6.3
77	Lißberg	9.09	50.38	220	9	9	56.5	69.8	305.9	2.9	70.9	56.0	7.3
29	Hirzenhain	9.13	50.39	250	7	10	163.9	-75.0	344.1	3.3	157.4	-75.6	7.8
28	Hirzenhain	9.14	50.40	255	10	12	201.9	-75.5	297.6	2.8	224.3	-72.8	8.1
31	Ortenberg	9.05	50.36	130	6	10	26.5	56.4	389.5	3.4	124.0	66.9	4.7
30	Ortenberg	9.09	50.36	280	9	10	200.7	-54.8	749.6	1.9	316.3	-68.8	3.7
113	Bergheim	9.11	50.34	296	9	10	139.2	-57.1	122.7	4.7	91.4	-58.8	9.9
115	Bergheim ^c	9.11	50.34	306	5	7	101.6	-58.4	501.2	3.4	119.6	-35.8	4.9
116	Bergheim ^a	9.11	50.34	311	10	11	194.3	-54.7	349.5	2.6	328.8	-71.8	5.0
117	Bergheim ^a	9.11	50.34	350	10	10	195.7	-56.0	481.3	2.2	323.5	-72.2	4.6
182	<i>DGI3</i> (V116 + 117)			331	20	21	195.0	-55.3	411.4	1.6	326.2	-72.0	4.7
76	Michelau	9.16	50.31	300	20	25	359.1	71.9	261.3	2.0	4.2	83.2	8.3
163	Michelau	9.16	50.31	324	7	10	10.8	66.1	437.0	2.9	108.8	82.7	6.1
101	Birstein	9.30	50.35	283	16	17	352.6	36.1	57.7	4.9	203.1	59.4	10.5
104	Kerbersdorf	9.38	50.33	234	8	9	191.6	-76.1	729.5	2.1	209.9	-75.3	5.3
16	Kerbersdorf	9.38	50.33	250	10	10	164.6	-75.2	220.4	3.3	160.3	-75.2	9.4
17	Kerbersdorf ^b	9.38	50.34	258	12	23	146.1	-30.7	68.3	5.3	60.6	-47.0	6.9
19	Schönhof	9.37	50.34	308	28	30	195.5	-60.4	366.6	1.4	313.0	-76.0	5.7
18	Schönhof	9.38	50.35	320	13	13	340.7	72.1	175.1	3.1	319.0	76.6	10.0
15	Marborn	9.40	50.32	350	10	12	180.7	-80.0	190.4	3.5	190.2	-69.5	10.8
167	Kressenbach	9.46	50.35	289	6	9	356.8	40.5	85.6	7.3	195.9	62.8	9.0
164	Kressenbach	9.45	50.38	297	6	10	347.7	50.8	882.5	2.3	219.9	69.1	2.9
165	Kressenbach	9.45	50.35	375	10	10	179.3	-52.8	726.9	1.8	11.5	-73.1	3.4
166	Kressenbach	9.45	50.35	393	11	12	350.2	74.0	402.8	2.3	344.1	78.8	7.0
105	Breitenbach	9.48	50.38	420	6	9	184.6	-64.0	351.8	3.6	333.0	-84.6	5.6
73	Calbach	9.05	50.28	209	8	9	211.5	-63.9	996.0	1.8	279.2	-68.6	3.7
75	Calbach	9.05	50.28	217	9	11	206.2	-66.1	1,362.2	1.4	274.8	-72.9	3.4
119	Breitenborn	9.21	50.28	370	10	10	10.3	62.0	1,707.9	1.2	140.0	80.1	2.9
118	Breitenborn ^a	9.21	50.28	383	12	12	71.6	54.3	313.6	2.5	87.1	37.3	5.1
120	Breitenborn ^a	9.21	50.28	391	9	10	68.3	55.5	459.6	2.4	88.1	40.0	4.9
183	<i>DGI4</i> (V118 + 120) ^c			387	21	22	70.2	54.8	354.1	1.7	87.5	38.5	5.1

Note. The different columns represent: the site (or group) number; the name of the locality; the longitude (Slon), latitude (Slat), and altitude (Salt) of the site; the number *n* (*N*) of interpreted (measured) samples per site; the declination (D_g) and inclination (I_g) in geographic coordinates together with the precision parameter (*k*) and the 95% confidence radius (α_{95}); the longitude (Plon_g) and latitude (Plat_g) of the virtual geomagnetic poles in geographic coordinates together with the within-site dispersion S_w . ^aCombined into the directional groups (DGs) highlighted in italics. ^bDetected as transitional with an adaptive (Vandamme, 1994) VGP cutoff. ^cDetected as transitional with both 45° and adaptive VGP cutoff. More details about the sites can be found in Table S2.

Table 2
Average Paleomagnetic Directions and Poles

	N	D_g	I_g	k	α_{95}	$Plon_g$	$Plat_g$	K	A_{95}
Sites ¹ , combined polarity	135	4.1	62.7	31.1	2.2	155.5	84.8	18.5	2.9
Sites ¹ , normal polarity	63	6.1	62.1	34.9	3.1	148.5	83.3	21.0	4.0
Sites ¹ , reversed polarity	72	2.3	63.2	28.3	3.2	166.1	86.1	16.7	4.2
Sites ¹ , group 1	30	3.8	63.1	41.3	4.1	155.4	84.8	25.0	5.4
Sites ¹ , group 2	46	2.6	60.6	28.3	4.0	173.6	82.9	18.0	5.1
Sites ¹ , group 3	30	3.5	64.0	34.0	4.6	154.8	86.3	18.3	6.3
Sites ¹ , group 4	29	7.8	64.5	25.6	5.4	114.1	84.7	14.8	7.2
DGs², combined polarity	116	3.8	62.2	30.2	2.4	161.9	84.5	18.2	3.2
DGs ² , normal polarity	54	5.3	61.3	32.2	3.5	156.9	82.9	19.6	4.5
DGs ² , reversed polarity	62	2.3	63.1	28.5	3.4	169.5	85.9	17.0	4.5
DGs ² , $k \geq 50$	115	3.8	62.3	30.0	2.4	161.0	84.6	18.1	3.2
DGs ² , $k \geq 100$	112	4.3	63.0	31.8	2.4	155.1	85.1	18.5	3.2
Sherwood (1990)	33	357.6	63.2	20.5	5.7	217.9	86.2	12.2	7.5
APWP BC02 ³ @10 Ma	54	3.0	64.5			162.5	85.4		2.0
APWP BC02 ³ @20 Ma	38	4.8	63.8			154.8	84.0		2.7
APWP Tor12 ⁴ @10 Ma	49	3.1	65.7			150.0	86.7		1.8
APWP To12 ⁴ @20 Ma	31	4.9	64.2			152.1	84.4		2.6
APWP Va23 ⁵ @10 Ma		2.5	66.5			141.4	87.8		1.3
APWP Va23 ⁵ @20 Ma		3.2	62.9			168.7	83.5		1.1

Note. The different columns represent: The selected data set or subset; the number N of directions used to compute the average; the declination (D_g) and inclination (I_g) in geographic coordinates together with the precision parameter (k) and the 95% confidence radius (α_{95}); the longitude ($Plon_g$) and latitude ($Plat_g$) of the virtual geomagnetic poles in geographic coordinates together with the precision parameter (K) and the 95% confidence radius (A_{95}). The results from this study, before¹ and after² the construction of the directional groups (DGs), are compared with the previous results by Sherwood (1990), and with the apparent polar wander paths (APWP) for stable Europe: ³Besse and Courtillot (2002, 2003), ⁴Torsvik et al. (2012), ⁵Vaes et al. (2023). Our preferred interpretation is highlighted in bold.

exceeding the critical value $\theta_C = 4.5^\circ$ to reject the null hypothesis of equality of the populations. At 5% significance level, the populations corresponding to each rock-magnetic group are statistically indistinguishable from the whole population (Table 2; Figure S4 in Supporting Information S1). While the variability in the rock-magnetic properties can be explained by the low- and/or high-temperature oxidation of titanomagnetite (e.g., Kontny et al., 2003), the absence of correlation between rock-magnetic properties and paleodirections most likely reflects that oxidation occurred during the initial cooling of the rocks and is not related to later alteration events (e.g., Shcherbakov et al., 2024).

To increase the robustness of the data set, we tested the presence of correlation (see Section 3.4) in the sequences of lava flows (Nieder-Ofleiden, Dreihausen, Brauerschwend, Londorf, Rudingshain, Widdersheim, Nidda, Rainrod, Schotten, Ortenberg/Bergheim, Calbach, Breitenborn; Table 1 and Figures 2a–2c) as well as for the volcanic units located in a radius of less than 5 km (Alten-Buseck, Allendorf, Almenrod, Lauterbach, Lanzenhain, Stockhausen, Gedern, Herchenhain, Hirzenhain, Michelau, Kerbersdorf, Kressenbach; Table 1). Irrespective of the used algorithm, we detected 21 correlated directions that were combined into 14 DGs (Table 1). Among the 127 directions/DGs thought to represent independent geomagnetic records, we detected 7 transitional directions with a fixed VGP cutoff ($A = 45^\circ$) and 11 transitional directions with an adaptive VGP cutoff ($A = 39.5^\circ$). Considering the case of an adaptive VGP cutoff (54 directions/DGs of normal polarity, 62 directions/DGs of reversed polarity; Figures 6d–6f), the conventional reversal test ($\theta = 2.3^\circ < \theta_C = 4.7^\circ$) as well as the bootstrap reversal test ($\lambda = 2.8 < \lambda_C = 12.6$) are both positive. At 5% significance level, the populations for $k \geq 50$ and $k \geq 100$ are statistically indistinguishable from the whole population (Table 2). We will thus rely on the whole population for the rest of the paper.

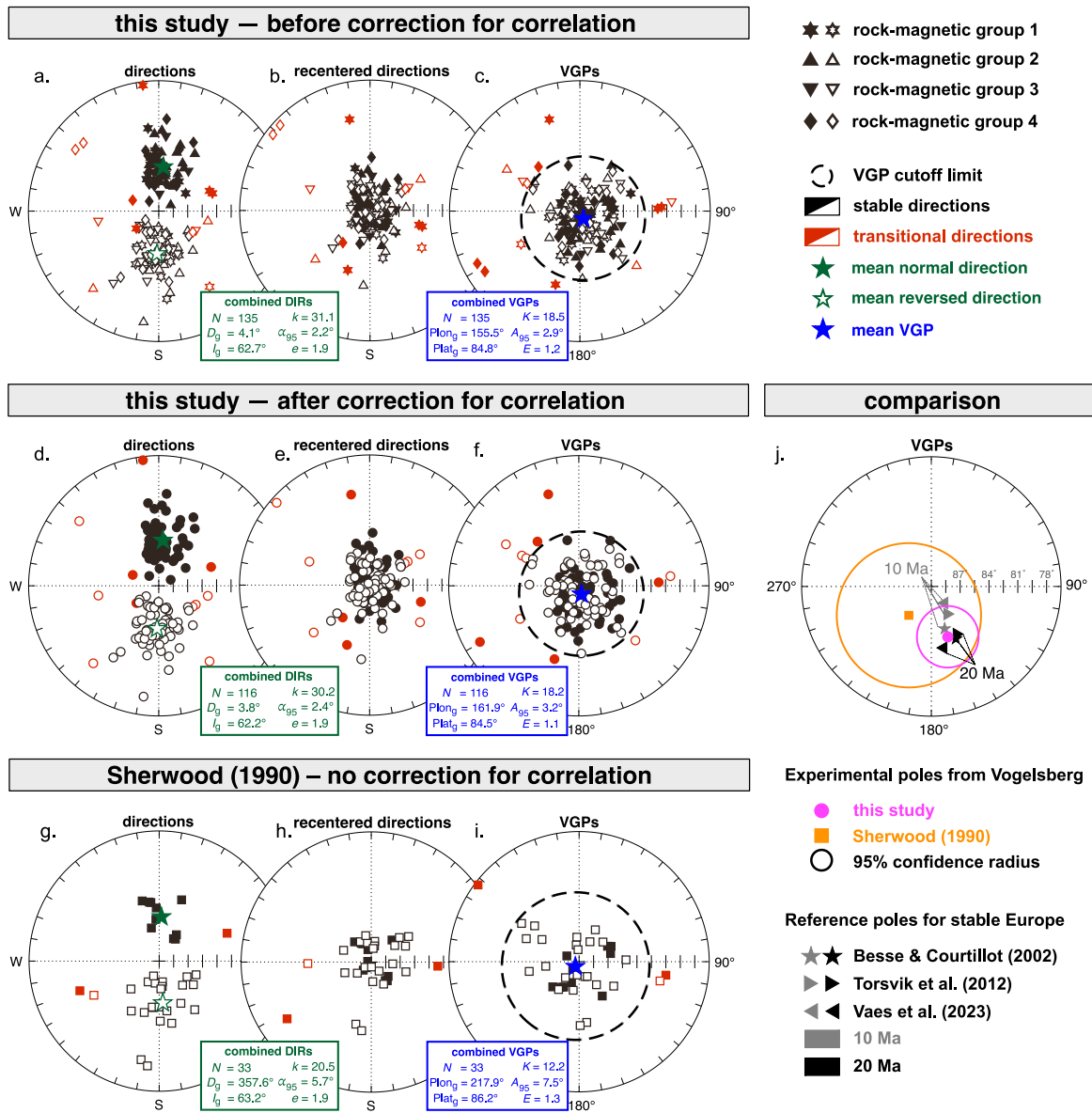


Figure 6. Paleodirectional results from the Vogelsberg. (a–c) Stereographic projection of the directions, recentered directions, and VGPs of the site averages in geographic coordinates. The different marker types stand for the rock-magnetic groups. (d–f) Stereographic projection of the directions, recentered directions and VGPs of the site-group averages in geographic coordinates. (g–i) Stereographic projection of the directions, recentered directions and VGPs of the site averages from Sherwood (1990) in geographic coordinates. For each panel, the red color marks the transitional sites (or site groups) detected with an adaptive VGP cutoff. For each inset, N is the number of stable sites/DGs; (D_g , I_g) or ($Plon_g$, $Plat_g$) correspond to the mean direction or mean VGP in geographic coordinates; (k , K) is the precision parameter of the distribution; (α_{95} , A_{95}) is the 95% confidence radius of the mean direction/VGP; (e , E) is the elongation parameter of the distribution. (j) Comparison of our paleomagnetic pole with the previous pole by Sherwood (1990), and with the reference poles for stable Europe (Besse & Courtillot, 2002; Torsvik et al., 2012; Vaes et al., 2023).

Among the 37 sites investigated by Sherwood (1990), we managed to resample and successfully interpret 23 sites. The angular distance between the pairs of site-mean directions lies in the interquartile range 1.8–8.0°, with a median of 3.8°. At the study level, our mean direction ($D_g = 3.8^\circ$, $I_g = 62.2^\circ$, $\alpha_{95} = 2.4^\circ$, $N = 116$, Figure 6d) is statistically indistinguishable from Sherwood (1990)'s direction ($D_g = 357.6^\circ$, $I_g = 63.2^\circ$, $\alpha_{95} = 5.7^\circ$, $N = 33$, Figure 6g), with $\theta = 2.0^\circ < \theta_C = 11.7^\circ$ for the conventional common mean test and $\lambda = 0.5 < \lambda_C = 12.7$ for the bootstrap common mean test. Our corresponding pole ($Plon_g = 161.9^\circ$, $Plat_g = 84.5^\circ$, $A_{95} = 3.2^\circ$, $N = 116$, Figure 6f) is also statistically indistinguishable from the reference pole for stable Europe at 20 Ma (Figure 6j), with an angular distance of 0.9° (Besse & Courtillot, 2002, 2003), 1.0° (Torsvik et al., 2012), and 1.2° (Vaes et al., 2023).

Table 3
Dispersion and Elongation of the Virtual Geomagnetic Poles (VPGs)

	45° Cutoff					Vandamme cutoff					
	<i>N</i>	<i>S_B</i>	<i>S_B⁻</i>	<i>S_B⁺</i>	<i>E</i>	<i>N</i>	<i>A</i>	<i>S_B</i>	<i>S_B⁻</i>	<i>S_B⁺</i>	<i>E</i>
Sites ¹ , all	139	20.0	18.3	21.9	1.1	135	39.2	18.9	17.4	20.6	1.2
Sites ¹ , <i>k</i> > 50	138	20.0	18.4	21.9	1.1	134	39.3	18.9	17.4	20.6	1.2
Sites ¹ , <i>k</i> > 100	134	19.6	17.9	21.4	1.2	130	38.4	18.5	17.0	20.1	1.0
DGs², all	120	20.3	18.5	22.3	1.2	116	39.5	19.1	17.5	20.8	1.1
DGs ² , <i>k</i> > 50	119	20.4	18.6	22.4	1.2	115	39.6	19.1	17.5	20.9	1.1
DGs ² , <i>k</i> > 100	115	19.9	18.1	21.9	1.4	112	39.2	18.9	17.3	20.7	1.2
DGs ² , normal	55	19.1	16.8	22.3	1.3	54	–	18.3	16.2	21.0	1.3
DGs ² , reversed	65	21.2	18.7	24.1	1.3	62	–	19.7	17.5	22.3	1.2
Sherwood (1990)	33	22.8	19.3	26.7	1.3	33	47.3	22.8	19.3	26.7	1.3
Jarboe et al. (2008)	71	20.2	18.0	22.5	2.2	71	41.7	20.2	18.0	22.5	2.2
Dominguez et al. (2014)	32	18.0	15.1	21.5	1.7	32	38.6	18.0	15.1	21.5	1.7

Note. For each data set, *N* is the number directions, *A* is the optimal cutoff angle, *S_B* is the angular standard deviation of the VPGs defined by Equation 1, [*S_B⁻*; *S_B⁺*] is the 95% confidence interval on *S_B*, *E* is the elongation parameter. The results from this study, before¹ and after² correction for serial correlation, are compared with the previous results by Sherwood (1990) for the Vogelsberg. Our results also compared with the coeval results from the Steens Basalt (15.5–17.2 Ma; Jarboe et al., 2008; Mankinen et al., 1985) and the Grande Ronde Basalt (15.0–15.6 Ma; Dominguez & Van der Voo, 2014) of the Columbia River Basalt Group (USA) emplaced at similar paleolatitude. Our preferred interpretation is highlighted in bold.

4.4. Estimates of the VGP Scatter

The VGP scatter is ~6% lower for an adaptive VGP cutoff than for a fixed VGP cutoff, as a direct consequence that the adaptive VGP cutoff removes more transitional directions than the fixed VGP cutoff (Table 3). Irrespective of the chosen cutoff method, *S_B* increase by 1%–2% after the removal of the serial correlations, which confirms that some directions were oversampled in the original data set. The quantity *S_B* decreases by 1%–2% when the directions/DGs with *k* < 100 are discarded. However, as these changes are negligible with respect to the individual uncertainties on *S_B*, we rely on the unfiltered data set of 116 (for an adaptive VGP cutoff) or 120 (for a fixed VGP cutoff) stable independent directions/DGs for our final interpretations. The data set for an adaptive VGP cutoff yields *S_B* = 19.1°_{17.5°}^{20.8°} (*N* = 116), the population of reversed polarity (*S_B* = 19.7°_{17.5°}^{22.3°}; *N* = 62) being more scattered than the population of normal polarity (*S_B* = 18.3°_{16.2°}^{21.0°}; *N* = 54). The populations of normal polarity (*E* = 1.3) and of reversed polarity (*E* = 1.2) are slightly more elongated than the population of combined polarity (*E* = 1.1), which indicates that the combined data set is probably more suitable for quantifying PSV.

To quantify the effect of increasing the number *N* of independent directional records on the values of *S_B* and *E*, we bootstrapped 10,000 pseudo-collections of VPGs from the original collection of 116 stable VPGs. For each value of *N* (from 10 to 116 in step of 5), we determined the mean values and 95% confidence intervals of *S_B* and *E* (Figure 7). For the VGP scatter, the average value of *S_B* is nearly invariant (to within 2%) as function of *N* (Figure 7a), confirming the absence of systematic bias on the value of *S_B*. However, the 95% confidence interval on *S_B* significantly decreases as function of *N*. It is reduced by a factor two when decreasing *N* from 10 to 35, by a factor three when decreasing *N* from 10 to 75. Increasing *N* above 75 only has a marginal effect on the confidence interval. For the elongation parameter, the average value of *E* significantly decreases as function of *N*, indicating the presence of a systematic bias for the present data set. The parameter *E* is overestimated by 122% at *N* = 10, by 22% at *N* = 35, and still by 5% at *N* = 75. In parallel, the 95% confidence interval on *E* decreases by 77% from *N* = 10 to *N* = 35, by 87% from *N* = 10 to *N* = 75. Like for *S_B*, increasing *N* above 75 only has a marginal effect on the confidence interval. As a conclusion, our data set consisting of 116 stable VPGs should provide reliable values of *S_B* and *E*. Larger uncertainties on *S_B* and *E* would arise on data sets with less than 50 stable VPGs, with a risk of strong bias on the value of *E*.

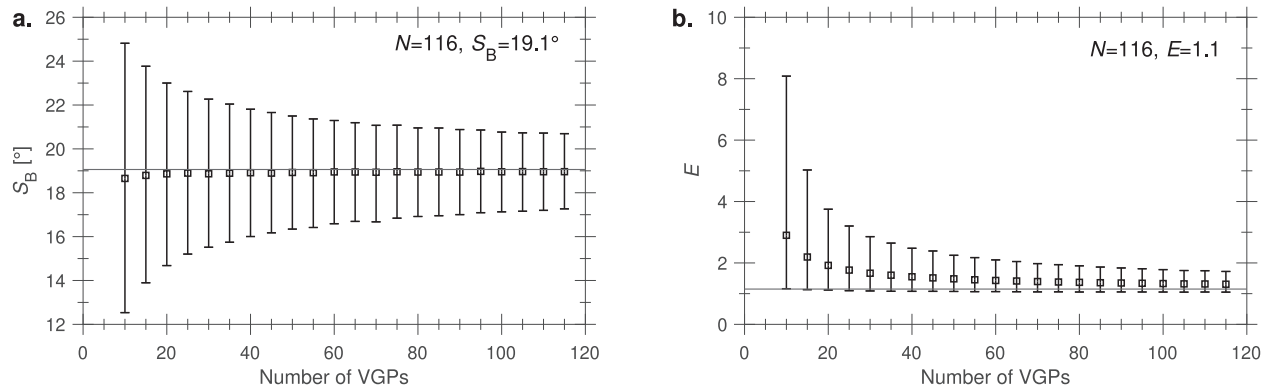


Figure 7. Convergence of the VGP scatter S_B (panel a) and of the elongation parameter E (panel b) as a function of the number N of independent paleomagnetic records. The mean value and 95% confidence interval of S_B and E were calculated from 10,000 pseudo collections of VGPs bootstrapped from the original collection of 116 stable VGPs for each value of N . The horizontal lines represent the empirical values of S_B and E for the original collection, also indicated in the upper right corner of the panels.

5. Discussion

5.1. Robustness of the Data Set

Starting from a collection of 1,920 samples out of 162 sites, we successfully determined the directions of 148 sites, which yielded 116 independent paleomagnetic records of stable polarity after removing between-site correlation and discarding the transitional sites. With an angular distance of 2.3° between the populations of normal and reversal polarity, this data set unambiguously passes the reversal test, which indicates that secondary overprints—mostly due to lightning strikes—were efficiently removed by AF demagnetization. Among the seven localities that were previously dated and investigated in this study, six of them yield a polarity consistent with the predictions of the GPTS (Table S1; Ogg, 2020). Additionally, the 10 paleomagnetic sites from the Londorf sequence yield normal polarities, consistent with the predictions from the GPTS for two of the available ages. The inconsistency with the two other available ages from the Londorf sequence (sample VB 97–113 from Bogaard et al., 2001; sample #2 from Harre et al., 1975; Table S1) may be explained by the uncertainties on the age determinations exceeding the chron boundaries and/or by the fact that we did not sample the same lava flows.

Our mean direction is statistically indistinguishable from the mean direction obtained in the previous paleomagnetic survey of Vogelsberg by Sherwood (1990). However, by almost quadrupling the number of available paleomagnetic readings, we obtain a distribution of paleodirections more suitable for the investigation of PSV. First of all, the distribution of directions from Sherwood (1990) was anomalously elongated in the equatorial plane; our distribution is elongated in the meridional plane, consistent with the axial dipolar field observed for the past 5 Myr (Tauxe & Kent, 2004). Second, by increasing the number of paleomagnetic records, we could halve the uncertainty on S_B , that is, reducing the 95% bootstrap uncertainty range from 7.4° to 3.3° . As noted in Section 4.3, our distribution of VGPs is $\sim 8\%$ more scattered for the population of reversed polarities ($N = 62$) than for the population of normal polarities ($N = 55$). This apparent asymmetry, already observed in Sherwood (1990), is likely the consequence that the geodynamo spent $\sim 50\%$ more time in a reversed state (4 chrons for a total duration of 1.43 Myr between 15.2 and 17.6 Ma) than in a normal state (4 chrons for a total duration of 0.94 Myr between 15.2 and 17.6 Ma) according to the GPTS (Ogg, 2020). From this viewpoint, PSV is probably better averaged for the population of reversed polarity than for the population of normal polarity.

Our data set is compatible with the apparent polar wander path for stable Europe, which indicates that the Vogelsberg has remained tectonically stable since its emplacement. Emplaced between 17.6 and 15.2 Ma at a magnetic latitude of 43.5°N (inclination of 62.2°N), the Vogelsberg from Central Europe can also be directly compared to the Columbia River Basalt Group from North America, the main activity of which occurred between 17.0 and 16 Ma (e.g., Kasbohm & Schoene, 2018). From the paleomagnetic data published by Dominguez and Van der Voo (2014) and covering a time interval from 15.6 to 6 Ma, we selected the records from the Grande Ronde and Wanapum formations emplaced prior to 15 Ma, 33 of which were determined on 5 or more samples per site and yield $k \geq 50$. From the paleomagnetic data in the Steens Mountain area covering a time interval from 17.2

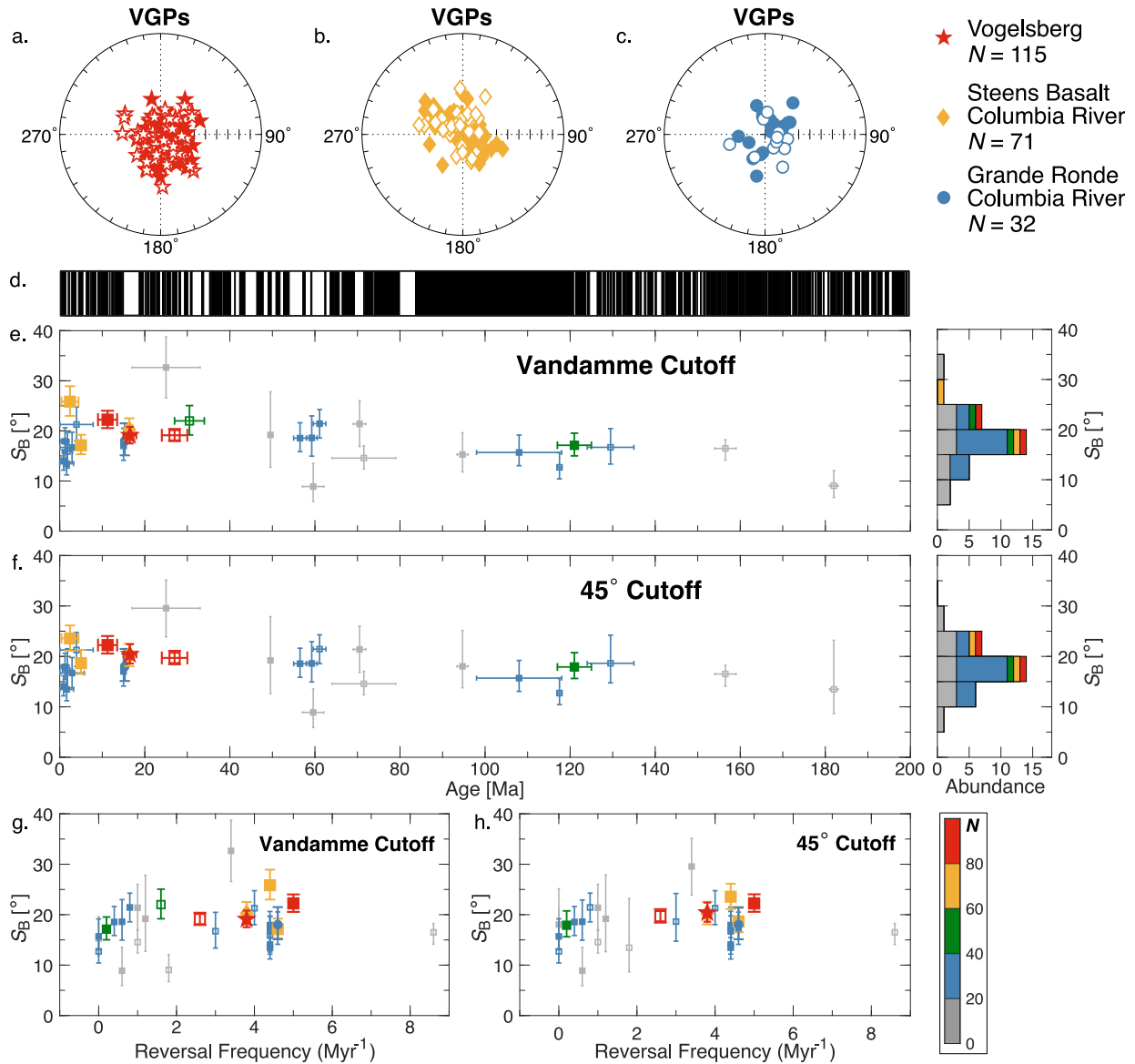


Figure 8. Analysis of the dispersion of the virtual geomagnetic poles (VGPs) at mid magnetic latitude (40–50°) over the past 200 Myr (see Table S5). (a–c) Stereographic projection of the distributions of stable VGPs from Vogelsberg (red stars, 15.2–16.6 Ma; this study), the Steens Basalt (yellow diamonds, 15.5–17.2 Ma; Jarboe et al., 2008; Mankinen et al., 1985) and the Grande Ronde Basalt (blue circles, 15.0–15.6 Ma; Dominguez & Van der Voo, 2014). (d) Geomagnetic polarity timescale (GPTS) showing periods of normal (resp. reverse) polarity in black (resp. white). C- and M-sequences from Ogg (2020). Composite sequence for the Jurassic from Hesselbo et al. (2020). (e–f) VGP scatter S_B as a function of age, using an adaptive (panel e; Vandamme, 1994) or 45° (panel f) VGP cutoff to remove transitional directions. (g–h) VGP scatter S_B as a function of reversal frequency estimated for a 5 Myr window centered about the average age of each data set. The color/size coding of the markers represents the number N of directions used to compute S_B .

to 15.5 Ma (Jarboe et al., 2008; Mankinen et al., 1985), we retained the 72 records satisfying the same selection criteria. Whatever the choice of the VGP cutoff to remove the transitional directions, the two data sets yield the estimates $S_B = 18.0^\circ_{15.1^\circ}$ ($N = 32$) and $S_B = 20.2^\circ_{18.0^\circ}$ ($N = 71$), which are to within the statistical uncertainties of the estimates indistinguishable from $S_B = 19.1^\circ_{17.5^\circ}$ ($N = 116$) for the Vogelsberg data set (Figure 8a; Table 3).

5.2. Temporal Evolution of the VGP Scatter at Mid-Latitude

Based on the assumption that the latitudinal dependency of S_B can be described by a two-parameter law $S_B(\lambda) = \sqrt{a^2 + (b\lambda)^2}$ (model G of McFadden et al., 1988), our estimate of S_B for the Vogelsberg can be

compared with the predictions of S_B at a magnetic latitude $\lambda = 43.5^\circ$ for different epochs. Our estimate $S_B = 19.1^{+20.8^\circ}_{-17.5^\circ}$ ($N = 116$) lies within the predicted range $S_B = 18.5^{+24.9^\circ}_{-13.0^\circ}$ for the Miocene, considering the equatorial value $a = 15.6^{+18.6^\circ}_{-13.0^\circ}$ and latitude-dependency parameter $b = 0.23^{+0.38}_{-0.00}$ proposed by Engbers et al. (2022). On the contrary, our estimate is greater than and does not intersect with the prediction $S_B = 13.7^{+17.2^\circ}_{-10.3^\circ}$ for the CNS, considering the preferred parameter values $a = 9.4^{+11.7^\circ}_{-7.1^\circ}$ and $b = 0.23^{+0.29}_{-0.16}$ proposed by Lhuillier et al. (2024). Finally, it is also greater than but marginally intersect with the prediction $S_B = 15.9^{+18.1^\circ}_{-13.4^\circ}$ for the past 10 Myr, considering the parameter values $a = 12.4^{+13.7^\circ}_{-10.9^\circ}$ and $b = 0.23^{+0.27}_{-0.18}$ proposed by de Oliveira et al. (2021). From this viewpoint, our estimate from the Vogelsberg would support a higher amplitude of PSV during the Miocene than during the past 10 Myr, as proposed by Engbers et al. (2022). However, given the large uncertainties on the parameters describing the latitudinal profile of S_B , we prefer analyzing all experimental estimates of S_B at mid magnetic latitude ($40\text{--}50^\circ$) in the rest of the discussion.

By scanning the most recent palaeodirectional databases on volcanic rocks for the past 10 Myr (de Oliveira et al., 2021), for the Miocene (Engbers et al., 2022), for the Paleogene (Engbers et al., 2024), and for the Cretaceous and the Jurassic (Dobrovine et al., 2019), we identified 28 data sets in the desired range of magnetic latitude ($40\text{--}50^\circ$), with at least 10 independent directions per data set (Table S4). We added to this collection our data set for the Vogelsberg as well as the recent data set for the Oaş–Gutâi Mountains in Romania (A. G. Panaiotu & Kovacs, 2024). Starting from the original site-mean data of the publications and following the authors' prescriptions for the removal of the serial correlations, we first selected the records with five samples or more per site and $k \geq 50$. From these filtered data sets, we then computed the VGP scatter S_B after the removal of the transitional directions with a fixed (45°) or adaptive (Vandamme, 1994) VGP cutoff.

When representing S_B as a function of age, we could not identify any clear trend, irrespective of the choice of the VGP cutoff (Figures 8e and 8f). Among the 30 available data sets, 22 (resp. 8) of them consist of less than 40 (resp. 20) independent stable directions. These data sets are characterized by large uncertainties on S_B (and sometimes also on age), making them not ideal for investigating PSV. On the contrary, three well-dated data sets consist of more than 80 independent stable directions: the one for the Kerguelen archipelago (24–30 Ma; Camps et al., 2007), the one for the Vogelsberg (15.2–17.6 Ma; this study), and the one for Oaş–Gutâi Mountains in Romania (9–13.5 Ma; A. G. Panaiotu & Kovacs, 2024). Additionally, three data sets, consisting of 60–80 independent stable directions, are also well suited for investigating PSV: the one for the Steens Basalt in the USA (15.5–17.2 Ma; Jarboe et al., 2008; Mankinen et al., 1985), the one for the North Harguita Mountains in Romania (4–6 Ma; Vişan et al., 2016), and the one for the South Harguita Mountains in Romania (0.4–4.4 Ma; C. G. Panaiotu et al., 2012). To be more quantitative, we represented S_B as a function of reversal frequency f_{rev} estimated for a 5 Myr window centered about the average age of each data set (Figures 8g and 8h). In the absence of filtering, the Pearson correlation R between S_B and f_{rev} is on the order of +18%, yet statistically insignificant with a p -value P of 0.35 (0.35) for the adaptive (fixed) VGP cutoff. Generally, R tends to increase when the number N of individual stable directions per data set increases. The highest correlation is found for $N \geq 40$, with $R = 37\%$ (65%) but $P = 0.37$ (0.12) for the adaptive (fixed) VGP cutoff. As a conclusion, for the present investigation at mid magnetic latitude ($40\text{--}50^\circ$), a positive correlation between S_B and f_{rev} may be hypothesized, consistent with the predictions of numerical dynamo simulations (e.g., Lhuillier & Gilder, 2013). However, this correlation is statistically insignificant whatever the filtering scenario. Whether the failure of the correlation is due to (a) the insufficient number of data sets with $N \geq 50\text{--}100$, (b) the uncertainty on the ages of the data sets, or (c) a working of the geodynamo more complicated than expected, remains an open question.

6. Conclusions

1. A comprehensive rock-magnetic and paleodirectional investigation was conducted on 162 volcanic units (1920 paleomagnetic cores) from the Vogelsberg (Germany), emplaced between 17.6 and 15.2 Ma.
2. The paleodirections from 148 volcanic units, reduced to 127 independent directions after correction for serial correlation, were successfully interpreted.
3. Despite the wide variability in the titanium content of the titanomagnetite grains, no correlation was found between the rock-magnetic properties and the paleodirections. This observation points to deuteric oxidation of the titanomagnetite grains.

4. After the removal of the transitional directions, the average direction is located at $D_g = 3.8^\circ$, $I_g = 62.2^\circ$ ($\alpha_{95} = 2.4^\circ$, $N = 116$) and the average pole at 161.9°E , 84.5°N ($A_{95} = 3.2^\circ$, $N = 116$). These values, reflecting a paleolatitude of $\sim 43.5^\circ$, are consistent with the apparent polar wander path for stable Europe.
5. Our robust estimate of the VGP scatter $S_B = 19.1^{+20.8}_{-17.5}$ ($N = 116$) halves the uncertainty of the previous estimate of S_B obtained by Sherwood (1990). This value may be suggestive of a more variable paleomagnetic field during the Miocene relative to the past 10 Myr (Engbers et al., 2022).
6. The paleomagnetic data sets at a magnetic latitude of $40\text{--}50^\circ$ over the past 200 Myr are inconsistent with a correlation between S_B and the reversal rate in this latitudinal range. This result contradicts the predictions from numerical dynamo simulations (Lhuillier & Gilder, 2013).

Data Availability Statement

The demagnetization data and fitted directions are available in the MagIC database (Chi & Lhuillier, 2025).

Acknowledgments

This study was supported by the Deutsche Forschungsgemeinschaft (DFG, German Research Foundation)—Projektnummer 517539177. Y.C. acknowledges the financial support by the China Scholarship Council (CSC)—Grant 202208080269. We thank Michael Eitel, Sandra Elisabeth Hahn, Felix Ostermeier, Darsana Lekshmy Raj, Maria Rosalita Pujiastuti Sudibyo, and Donata Nariswari Wahyu Wardani for their help during the field campaigns. We thank Mitteldeutsche Hartstein-Industrie AG for giving us access to the quarries of Allendorf, Bergheim, Brauerschwend, Breitenborn, Dreihausen, Nieder-Ofleiden, and Widersheim; Weimer GmbH for giving us access to the quarries of Nidda (“Im Liebhölzchen”) and Großen-Buseck (“Am Kahlenberg”); Glock Steinbruch und Erdponie GmbH for giving us access to the quarry of Calbach; Basalt- & Betonwerk Eltersberg GmbH & Co. KG for giving us access to the quarry of Alten-Buseck; Reinhard Bischoff for leaving us drilling the outcrops in his garden in Rainrod. We thank Mark Dekkers and Agnes Kontny for editorial handling; Daniel Pastor-Galán and an anonymous reviewer for their constructive comments. Open Access funding enabled and organized by Projekt DEAL.

References

- Alken, P., Thébault, E., Beggan, C. D., Amit, H., Aubert, J., Baerenzung, J., et al. (2021). International geomagnetic reference field: The thirteenth generation. *Earth Planets and Space*, 73(1), 49. <https://doi.org/10.1186/s40623-020-01288-x>
- Angenheister, G. (1956). Über die Magnetisierung der Basalte des Vogelsberges. *Nachrichten der Akademie der Wissenschaften in Göttingen, Mathematisch-Physikalische Klasse*, 9, 187–204.
- Angenheister, G., & Turkowsky, C. (1964). Die Verteilung der induzierten und natürlichen remanenten Magnetisierung innerhalb einiger Basaltlagen des Vogelsberges. *Bollettino di Geofisica Teorica ed Applicata*, 6(24), 285–295.
- Besse, J., & Courtillot, V. (2002). Apparent and true polar wander and the geometry of the geomagnetic field over the last 200 Myr. *Journal of Geophysical Research*, 107(B11), 2300. <https://doi.org/10.1029/2000JB000050>
- Besse, J., & Courtillot, V. (2003). Correction to “Apparent and true polar wander and the geometry of the geomagnetic field over the last 200 Myr”. *Journal of Geophysical Research*, 108(B10), 2469. <https://doi.org/10.1029/2003JB002684>
- Bogaard, P. J. F., & Wörner, G. (2003). Petrogenesis of basaltic to tholeiitic volcanic rocks from the Miocene Vogelsberg, Central Germany. *Journal of Petrology*, 44(3), 569–602. <https://doi.org/10.1093/ptrology/44.3.569>
- Bogaard, P. J. F., Wörner, G., & Henjes-Kunst, F. (2001). Chemical stratigraphy and origin of volcanic rocks from the drill core “Forschungsborung Vogelsberg 1996. *Geologische Abhandlungen Hessen*, 107, 69–99.
- Böhlke, J. K., de Laeter, J. R., De Bièvre, P., Hidaka, H., Peiser, H. S., Rosman, K. J. R., & Taylor, P. D. P. (2005). Isotopic compositions of the elements, 2001. *Journal of Physical and Chemical Reference Data*, 34(1), 57–67. <https://doi.org/10.1063/1.1836764>
- Bourgeois, O., Ford, M., Diraison, M., Le Carlier de Veslud, C., Gerbault, M., Pik, R., et al. (2007). Separation of rifting and lithospheric folding signatures in the NW-Alpine foreland. *International Journal of Earth Sciences*, 96(6), 1003–1031. <https://doi.org/10.1007/s00531-007-0202-2>
- Camps, P., Henry, B., Nicolaysen, K., & Plenier, G. (2007). Statistical properties of paleomagnetic directions in Kerguelen lava flows: Implications for the late Oligocene paleomagnetic field. *Journal of Geophysical Research*, 112(B6), B06102. <https://doi.org/10.1029/2006jb004648>
- Chenet, A.-L., Fluteau, F., Courtillot, V., Gérard, M., & Subbarao, K. V. (2008). Determination of rapid Deccan eruptions across the Cretaceous-Tertiary boundary using paleomagnetic secular variation: Results from a 1200-m-thick section in the Mahabaleshwar escarpment. *Journal of Geophysical Research*, 113(B4), B04101. <https://doi.org/10.1029/2006JB004635>
- Chi, Y., & Lhuillier, F. (2025). Paleomagnetic secular variation of early-middle Miocene volcanics from Vogelsberg (Germany) [Dataset]. *Magnetics Information Consortium*. <https://doi.org/10.7288/V4/MAGIC/20252>
- Cox, A. (1970). Latitude dependence of the angular dispersion of the geomagnetic field. *Geophysical Journal of the Royal Astronomical Society*, 20(3), 253–269. <https://doi.org/10.1111/j.1365-246X.1970.tb06069.x>
- Cromwell, G., Johnson, C. L., Tauxe, L., Constable, C. G., & Jarboe, N. A. (2018). PSV10: A global data set for 0–10 Ma time-averaged field and paleosecular variation studies. *Geochemistry, Geophysics, Geosystems*, 19(5), 1533–1558. <https://doi.org/10.1002/2017GC007318>
- Day, R., Fuller, M. D., & Schmidt, V. A. (1977). Hysteresis properties of titanomagnetites: Grain-size and compositional dependence. *Physics of the Earth and Planetary Interiors*, 13(4), 260–267. [https://doi.org/10.1016/0031-9201\(77\)90108-X](https://doi.org/10.1016/0031-9201(77)90108-X)
- de Oliveira, W. P., Hartmann, G. A., Terra-Nova, F., Brandt, D., Biggin, A. J., Engbers, Y. A., et al. (2021). Paleosecular variation and the time-averaged geomagnetic field since 10 Ma. *Geochemistry, Geophysics, Geosystems*, 22(10), e2021GC010063. <https://doi.org/10.1029/2021gc010063>
- Dominguez, A. R., & Van der Voo, R. (2014). Secular variation of the middle and late Miocene geomagnetic field recorded by the Columbia River Basalt Group in Oregon, Idaho and Washington, USA. *Geophysical Journal International*, 197(3), 1299–1320. <https://doi.org/10.1093/gji/ggt487>
- Dobrovine, P. V., Veikkolainen, T., Pesonen, L. J., Piispa, E., Ots, S., Smirnov, A. V., et al. (2019). Latitude dependence of geomagnetic paleosecular variation and its relation to the frequency of magnetic reversals: Observations from the Cretaceous and Jurassic. *Geochemistry, Geophysics, Geosystems*, 20(3), 1240–1279. <https://doi.org/10.1029/2018GC007863>
- Dunlop, D. J. (2002). Theory and application of the Day plot (Mrs/Ms versus Hcr/Hc) 1. Theoretical curves and tests using titanomagnetite data. *Journal of Geophysical Research*, 107(B3), 2056. <https://doi.org/10.1029/2001JB000486>
- Ehrenberg, K.-H., Fromm, K., Grubbe, K., Harre, W., Hentschel, G., Hötling, B., et al. (1981). *Forschungsborungen im Hohen Vogelsberg (Hessen) Bohrung 1 (Flösser-Schneise) Bohrung 2/2A (Hasselborn)* (Vol. 81). Geologische Abhandlungen Hessen.
- Engbers, Y. A., Bono, R. K., & Biggin, A. J. (2022). PSVM: A global database for the Miocene indicating elevated paleosecular variation relative to the last 10 Myrs. *Geochemistry, Geophysics, Geosystems*, 23(8), e2022GC010480. <https://doi.org/10.1029/2022gc010480>
- Engbers, Y. A., Thallner, D., Bono, R. K., Sprain, C. J., Murray, M. J., Bristol, K., et al. (2024). A global paleosecular variation database for the Paleogene: Stationary secular variation behavior since the triassic? *Geochemistry, Geophysics, Geosystems*, 25(6), e2023GC011203. <https://doi.org/10.1029/2023gc011203>
- Fabian, K., Shcherbakov, V. P., & McEnroe, S. A. (2013). Measuring the Curie temperature. *Geochemistry, Geophysics, Geosystems*, 14(4), 947–961. <https://doi.org/10.1029/2012GC004440>

- Fisher, R. (1953). Dispersion on a sphere. *Proceedings of the Royal Society of London Series A*, 217(1130), 295–305. <https://doi.org/10.1098/rspa.1953.0064>
- Gallet, Y., & Hulot, G. (1997). Stationary and nonstationary behaviour within the geomagnetic polarity time scale. *Geophysical Research Letters*, 24(15), 1875–1878. <https://doi.org/10.1029/97GL01819>
- Gallet, Y., & Pavlov, V. E. (2016). Three distinct reversing modes in the geodynamo. *Izvestiya - Physics of the Solid Earth*, 52(2), 291–296. <https://doi.org/10.1134/S106935131602004X>
- Harre, W., Kreuzer, H., Müller, H., Pucher, R., & Schricke, W. (1975). Datierungen nach der K/Ar-Methode und Paläomagnetik. In W. Schricke (Ed.), *Erläuterungen zur Geologischen Karte von Hessen 1:25000, Blatt Nr. 5319 Lendorf* (pp. 67–73). Hessisches Landesamt für Bodenforschung.
- Heslop, D., Sealey, J. L., Wood, A. T. A., Tauxe, L., & Roberts, A. P. (2023). A bootstrap common mean direction test. *Journal of Geophysical Research: Solid Earth*, 128(8), e2023JB026983. <https://doi.org/10.1029/2023jb026983>
- Hesselbo, S. P., Ogg, J. G., Ruhl, M., Hinnov, L. A., & Huang, C. J. (2020). The Jurassic period. In F. M. Gradstein, J. G. Ogg, M. D. Schmitz, & G. M. Ogg (Eds.), *Geologic time scale 2020* (pp. 955–1021).
- Hofbauer, G. (2021). *Vulkane in Deutschland*. wbg Theiss.
- Jarboe, N. A., Coe, R. S., Renne, P. R., Glen, J. M. G., & Mankinen, E. A. (2008). Quickly erupted volcanic sections of the Steens Basalt, Columbia River Basalt group: Secular variation, tectonic rotation, and the Steens Mountain reversal. *Geochemistry, Geophysics, Geosystems*, 9(11), Q11010. <https://doi.org/10.1029/2008gc002067>
- Johnson, C. L., & McFadden, P. L. (2015). The time-averaged field and paleosecular variation. In M. Kono (Ed.), *Geomagnetism* (pp. 385–417). Elsevier.
- Kasbohm, J., & Schoene, B. (2018). Rapid eruption of the Columbia River flood basalt and correlation with the mid-Miocene climate optimum. *Science Advances*, 4(9), eaat8223. <https://doi.org/10.1126/sciadv.aat8223>
- Kirschvink, J. L. (1980). The least-squares line and plane and the analysis of palaeomagnetic data. *Geophysical Journal of the Royal Astronomical Society*, 62(3), 699–718. <https://doi.org/10.1111/j.1365-246X.1980.tb02601.x>
- Koenigsberger, J. G. (1938). Natural residual magnetism of eruptive rocks. *Journal of Geophysical Research*, 43(3), 299–320. <https://doi.org/10.1029/TE043i003p00299>
- Kontny, A., Vahle, C., & de Wall, H. (2003). Characteristic magnetic behavior of subaerial and submarine lava units from the Hawaiian Scientific Drilling Project (HSDP-2). *Geochemistry, Geophysics, Geosystems*, 4(2), 8703. <https://doi.org/10.1029/2002gc000304>
- Koymans, M. R., Hinsbergen, D. J. J., Pastor-Galán, D., Vaes, B., & Langereis, C. G. (2020). Towards FAIR paleomagnetic data management through Paleomagnetism.org 2.0. *Geochemistry, Geophysics, Geosystems*, 21(2). <https://doi.org/10.1029/2019gc008838>
- Koymans, M. R., Langereis, C. G., Pastor-Galán, D., & van Hinsbergen, D. J. J. (2016). Paleomagnetism.org: An online multi-platform open source environment for paleomagnetic data analysis. *Computers & Geosciences*, 93(C), 127–137. <https://doi.org/10.1016/j.cageo.2016.05.007>
- Kreuzer, H., Besang, C., Harre, W., Müller, P., Ulrich, H.-J., & Vinken, R. (1973). K/Ar-Datierungen an jungtertiären Basalten aus dem Vogelsberg und aus dem Raum zwischen Kassel und Göttingen. *Fortschritte der Mineralogie*, 50(3), 10–11.
- Kreuzer, H., Kunz, K., Müller, P., Schenk, E., Harre, W., & Raschka, H. (1974). Petrologie und Kalium/Argon-Daten einiger Basalte aus der Bohrung 31, Rainrod I (Vogelsberg). *Geologisches Jahrbuch*, D(9), 67–84.
- Lhuillier, F., & Gilder, S. A. (2013). Quantifying paleosecular variation: Insights from numerical dynamo simulations. *Earth and Planetary Science Letters*, 382, 87–97. <https://doi.org/10.1016/j.epsl.2013.08.048>
- Lhuillier, F., & Gilder, S. A. (2019). Palaeomagnetism and geochronology of Oligocene and Miocene volcanic sections from Ethiopia: Geomagnetic variability in the Afro-Arabian region over the past 30 Ma. *Geophysical Journal International*, 216(2), 1446–1481. <https://doi.org/10.1093/gji/ggy517>
- Lhuillier, F., Lebedev, I. E., Tikhomirov, P. L., & Pavlov, V. E. (2024). High-latitude geomagnetic secular variation at the end of the Cretaceous normal superchron recorded by volcanic flows from the Okhotsk-Chukotka volcanic belt. *Journal of Geophysical Research: Solid Earth*, 129(1), e2023JB027550. <https://doi.org/10.1029/2023jb027550>
- Lhuillier, F., Shcherbakov, V. P., Gilder, S. A., & Hagstrum, J. T. (2017). Variability of the 0–3 Ma palaeomagnetic field observed from the boring volcanic field of the Pacific Northwest. *Geophysical Journal International*, 211(1), 69–79. <https://doi.org/10.1093/gji/ggx288>
- Lippolt, H. J., Todt, W., & Horn, P. (1974). Apparent potassium-argon ages of lower tertiary rhine graben volcanics. In J. H. Illies & K. Fuchs (Eds.), *Approaches to taphrogenesis*. E. Schweizerbart'sche Verlagsbuchhandlung.
- Lustrino, M., & Carminati, E. (2007). Phantom plumes in Europe and the circum-Mediterranean region. In G. R. Foulger & D. M. Jurdy (Eds.), *Plates, plumes and planetary processes* (Vol. 430, pp. 723–745). Geological Society of America. [https://doi.org/10.1130/2007.2430\(33\)](https://doi.org/10.1130/2007.2430(33))
- Mankinen, E. A., Prévot, M., Grommé, C. S., & Coe, R. S. (1985). The Steens Mountain (Oregon) geomagnetic polarity transition: 1. Directional history, duration of episodes, and rock magnetism. *Journal of Geophysical Research*, 90(B12), 10393–10416. <https://doi.org/10.1029/JB090iB12p10393>
- McElhinny, M. W. (2007). Geocentric axial dipole hypothesis. In D. Gubbins & E. Herrero-Bervera (Eds.), *Encyclopedia of geomagnetism and paleomagnetism* (pp. 281–287). Springer.
- McElhinny, M. W., & McFadden, P. L. (1997). Palaeosecular variation over the past 5 Myr based on a new generalized database. *Geophysical Journal International*, 131(2), 240–252. <https://doi.org/10.1111/j.1365-246X.1997.tb01219.x>
- McFadden, P. L., & McElhinny, M. W. (1990). Classification of the reversal test in palaeomagnetism. *Geophysical Journal International*, 103(3), 725–729. <https://doi.org/10.1111/j.1365-246X.1990.tb05683.x>
- McFadden, P. L., & Merrill, R. T. (1984). Lower mantle convection and geomagnetism. *Journal of Geophysical Research*, 89(B5), 3354–3362. <https://doi.org/10.1029/JB089iB05p03354>
- McFadden, P. L., Merrill, R. T., & McElhinny, M. W. (1988). Dipole/quadrupole family modeling of paleosecular variation. *Journal of Geophysical Research*, 93(B10), 11583–11588. <https://doi.org/10.1029/JB093iB10p11583>
- McFadden, P. L., Merrill, R. T., McElhinny, M. W., & Lee, S. (1991). Reversals of the Earth's magnetic field and temporal variations of the dynamo families. *Journal of Geophysical Research*, 96(B3), 3923–3933. <https://doi.org/10.1029/90JB02275>
- Merrill, R. T., McElhinny, M. W., & McFadden, P. L. (1996). *The magnetic field of the Earth: Paleomagnetism, the core, and the deep mantle* (2nd ed. Vol. 63). Academic Press.
- Min, K., Mundil, R., Renne, P. R., & Ludwig, K. R. (2000). A test for systematic errors in 40Ar/39Ar geochronology through comparison with U/Pb analysis of a 1.1-Ga rhyolite. *Geochimica et Cosmochimica Acta*, 64(1), 73–98. [https://doi.org/10.1016/S0016-7037\(99\)00204-5](https://doi.org/10.1016/S0016-7037(99)00204-5)
- Nairn, A. E. M. (1960). Paleomagnetic results from Europe. *The Journal of Geology*, 68(3), 285–306. <https://doi.org/10.1086/626660>
- Néel, L. (1955). Some theoretical aspects of rock-magnetism. *Advances in Physics*, 4(14), 191–243. <https://doi.org/10.1080/0018735500101204>
- Nesbor, H.-D. (2018). Das Vulkangebiet Vogelsberg. *Geologisches Jahrbuch Hessen*, 139, 5–41.

- Ogg, J. G. (2020). Geomagnetic polarity time scale. In F. M. Gradstein, J. G. Ogg, M. D. Schmitz, & G. M. Ogg (Eds.), *Geologic time scale 2020* (pp. 159–192).
- Panaiotu, A. G., & Kovacs, M. (2024). Paleomagnetism of the Miocene volcanism of the Oaş – Gutâi mountains revisited (eastern Carpathians, Romania). *Revue Roumaine de Géologie*, 68, 17–27. <https://doi.org/10.59277/RRG-RJG.2024.03>
- Panaiotu, C. G., Vişan, M., Ţugui, A., Seghedi, I., & Panaiotu, A. G. (2012). Palaeomagnetism of the South Harghita volcanic rocks of the East Carpathians: Implications for tectonic rotations and palaeosecular variation in the past 5 Ma. *Geophysical Journal International*, 189(1), 369–382. <https://doi.org/10.1111/j.1365-246X.2012.05394.x>
- Reischmann, T., & Schraft, A. (2010). *Der Vogelsberg - Geotope im größten Vulkangebiet Mitteleuropas* (2nd ed.). Wiesbaden: Hessisches Landesamt für Umwelt und Geologie.
- Ritter, J. R. R., Jordan, M., Christensen, U. R., & Achauer, U. (2001). A mantle plume below the Eifel volcanic fields, Germany. *Earth and Planetary Science Letters*, 186(1), 7–14. [https://doi.org/10.1016/S0012-821X\(01\)00226-6](https://doi.org/10.1016/S0012-821X(01)00226-6)
- Schnepf, E., Rolf, C., & Struck, J. (2001). Paläo- und gesteinsmagnetische Untersuchungen an Kernen der Forschungsbohrung Vogelsberg 1996. *Geologische Abhandlungen Hessen*, 107, 151–169.
- Shcherbakov, V. P., Lhuillier, F., Gribov, S. K., Tselmovich, V. A., & Aphinogenova, N. A. (2024). Potential bias in volcanic paleomagnetic records due to Superimposed chemical remanent magnetization. *Geophysical Research Letters*, 51(12), e2024GL109630. <https://doi.org/10.1029/2024gl109630>
- Sherwood, G. J. (1990). A paleomagnetic and rock magnetic study of Tertiary volcanics from the Vogelsberg (Germany). *Physics of the Earth and Planetary Interiors*, 62(1–2), 32–45. [https://doi.org/10.1016/0031-9201\(90\)90190-9](https://doi.org/10.1016/0031-9201(90)90190-9)
- Tarduno, J. A., Cottrell, R. D., & Smirnov, A. V. (2002). The Cretaceous superchron geodynamo: Observations near the tangent cylinder. *Proceedings of the National Academy of Sciences of the United States of America*, 99(22), 14020–14025. <https://doi.org/10.1073/pnas.222373499>
- Tauxe, L. (1998). *Paleomagnetic principles and practice*. Kluwer Academic Publishers.
- Tauxe, L., & Kent, D. V. (2004). A simplified statistical model for the geomagnetic field and the detection of shallow bias in paleomagnetic inclinations: Was the ancient magnetic field dipolar? In J. E. T. Channell, D. V. Kent, W. Lowrie, & J. G. Meert (Eds.), *Timescales of the paleomagnetic field* (pp. 101–115). AGU.
- Tauxe, L., Klystra, N., & Constable, C. (1991). Bootstrap statistics for paleomagnetic data. *Journal of Geophysical Research*, 96(B7), 11723–11740. <https://doi.org/10.1029/91JB00572>
- Torsvik, T. H., Van der Voo, R., Preeden, U., Mac Niocaill, C., Steinberger, B., Doubrovine, P. V., et al. (2012). Phanerozoic polar wander, palaeogeography and dynamics. *Earth-Science Reviews*, 114(3–4), 325–368. <https://doi.org/10.1016/j.earscirev.2012.06.007>
- Turk, P.-G., Lohse, H.-H., Schürmann, M., Furfmann, U., & Lippolt, H. J. (1984). Petrographische und Kalium-Argon-Untersuchungen an basischen tertiären Vulkaniten zwischen Westerwald und Vogelsberg. *Geologische Rundschau*, 73(2), 599–617.
- Vaes, B., van Hinsbergen, D. J. J., van de Lagemaat, S. H. A., van der Wiel, E., Lom, N., Advokaat, E. L., et al. (2023). A global apparent polar wander path for the last 320 Ma calculated from site-level paleomagnetic data. *Earth-Science Reviews*, 245, 104547. <https://doi.org/10.1016/j.earscirev.2023.104547>
- Vandamme, D. (1994). A new method to determine paleosecular variation. *Physics of the Earth and Planetary Interiors*, 85(1–2), 131–142. [https://doi.org/10.1016/0031-9201\(94\)90012-4](https://doi.org/10.1016/0031-9201(94)90012-4)
- Vişan, M., Panaiotu, C. G., Necula, C., & Dumitru, A. (2016). Palaeomagnetism of the upper Miocene- lower pliocene lavas from the east carpathians: Contribution to the paleosecular variation of geomagnetic field. *Scientific Reports*, 6(1), 23411. <https://doi.org/10.1038/srep23411>
- Wack, M. R., & Gilder, S. A. (2012). The SushiBar: An automated system for paleomagnetic investigations. *Geochemistry, Geophysics, Geo-systems*, 13(3), Q12Z38. <https://doi.org/10.1029/2011GC003985>
- Wang, D., & Van der Voo, R. (2004). The hysteresis properties of multidomain magnetite and titanomagnetite/titanomaghemite in mid-ocean ridge basalts. *Earth and Planetary Science Letters*, 220(1–2), 175–184. [https://doi.org/10.1016/S0012-821X\(04\)00052-4](https://doi.org/10.1016/S0012-821X(04)00052-4)
- Watson, G. S. (1983). Large sample theory of the Langevin distribution. *Journal of Statistical Planning and Inference*, 8(3), 245–256. [https://doi.org/10.1016/0378-3758\(83\)90043-5](https://doi.org/10.1016/0378-3758(83)90043-5)
- Wicht, J., & Sanchez, S. (2019). Advances in geodynamo modelling. *Geophysical & Astrophysical Fluid Dynamics*, 113(1–2), 2–50. <https://doi.org/10.1080/03091929.2019.1597074>
- Zijderveld, J. D. A. (1967). A.C. Demagnetization of rocks: Analysis of results. In D. Collinson, K. M. Creer, & S. K. Runcorn (Eds.), *Methods in paleomagnetism* (pp. 254–286). Elsevier.